State-Space Inflow Model Identification from Viscous Vortex Particle Method for Advanced Rotorcraft Configurations

Chengjian He and Monica Syal
Advanced Rotorcraft Technology, Inc.
Sunnyvale, CA 94085

Mark B. Tischler and Ondrej Juhasz
US Army Aviation Development Directorate
Moffett Field, CA 94035

Abstract

This paper describes the methodology that identifies a state-space rotor induced inflow model from first-principle based viscous Vortex Particle Method (VPM) simulation for flight dynamics and control applications. Modern advanced rotorcraft configurations usually involve multiple rotors (e.g., co-axial), fans, wings, etc. where the aerodynamic interaction can be significant under certain flight conditions. The paper presents a unified state-space inflow formulation that addresses the aerodynamic interaction that is well suited for flight dynamics analysis and control design applications. In implementation, the unified inflow model is derived through system identification using VPM simulation generated data. The usage of first-principle based VPM provides a solid approach in capturing important rotor wake physics. This includes both the wake distortion and wake diffusion that are essential for an accurate interactional wake solution, without relying on empirical modeling parameters (e.g., vortex core size and wake dissipation parameters, etc.). The methodology of inflow model identification was first validated with a single rotor where measured data are available. Good agreement of the identified model response with the measurements was obtained. The methodology was further evaluated with a co-axial rotor system. Excellent correlation of the identified model with original VPM simulation was also obtained in both hover and forward flight.

Nomenclature

L	Inflow influence coefficient matrix
M	Inflow apparent mass coefficient matrix
r	Non-dimensional blade radial position
t	Simulation time
V	Inflow mass flow parameter
$w(r,\psi,t)$	Rotor inflow over the rotor plane
$\vec{w}_{intf}$	Rotor induced interference velocity (off-rotor)
α_n^{mc}	Rotor inflow states (cosine components)
α_n^{ms}	Rotor inflow states (sine components)
$\phi_n^m(r)$	Inflow radial shape function
τ	Inflow time delay
τ_n^{mc}	Inflow forcing function (cosine components)
τ_n^{ms}	Inflow forcing function (sine components)

Introduction

Most existing state-space based finite-state inflow models (Refs.[1] and [2]) used in flight dynamics and control analysis were originally developed for a single rotor solution which limits their ability to be directly used for multiple rotor configurations. This is due to the lack of an effective means for accurately resolving the effects of mutual interaction between rotors, which can be significant for multiple rotor systems, such as a co-axial rotor configuration where the rotors stay very close to each other.

There has been development that extended the existing finite-state inflow model to a co-axial rotor system (e.g., Refs. [3] and [4]). There has also been research work that investigated the inflow model identification methodology to derive the state-space inflow model from a free wake method (e.g., Refs. [5] and [6]). The research and development has investigated the inflow model identification method and enriched our understanding of the problem. The current research aims at developing a unified state-space inflow model to better reflect the rotor wake physics that allows for the effect of tip vortex roll-up, the wake distortion and diffusion, and wake interaction for an accurate prediction of the inflow dynamics. The approach taken is to apply first-principle based viscous Vortex Particle Method (VPM) (Refs. [7] and [8]) for generating the inflow response data

---

and to adopt CIFER® (Ref. [9]) for identifying the state space inflow model. The viscous VPM solves the vorticity-velocity form of the Navier-Stokes equation for the rotorcraft wake dynamics. VPM has been extensively validated with measured data for rotor induced flow, performance, airloads, and aerodynamic interaction (Refs. [7], [8], [10], [11]). The VPM simulation can accurately predict both the downwash magnitude and variation trend for various rotor configurations, including single main rotor, co-axial, tandem, tiltrotor, etc. In addition, it has been validated for a broad range of flight conditions, such as hover (in or out of ground effect), forward flight, climb and descent, autorotation (including vortex ring state), as well as steady and maneuvering flight. Even with Navier-Stoke based vorticity dynamics formulation, VPM is computationally very efficient. For example, for a typical full blade element rotor helicopter simulation using VPM rotor wake solver, it takes only about 0.085 seconds to complete one full step simulation on a single desktop PC equipped with one consumer GPU graphical card. Therefore, it was used in this research to carry out rotor wake simulation for the frequency sweeps needed to generate the inflow response data for the state-space inflow model identification through CIFER®.

Unified State-Space Induced Inflow Model

The approach taken here is to first form a unified state-space rotor wake induced inflow model that covers multiple rotor systems with any number of arbitrarily configured rotors that may interfere aerodynamically. A state-space rotor induced inflow model for each of the rotors is formulated by unifying the dynamic equations that govern the rotor self-induced inflow states and output equations which address the mutual rotor interference. The introduction of the interference outputs allows for the effects of rotor mutual interference and, therefore, the model thus formulated is well suited for multiple rotor configurations and is also capable of computing the rotor interference on the fuselage and aerodynamic surfaces (such as horizontal surfaces and vertical fins, etc.). The inflow dynamics of a multiple rotor system are coupled through mutual interference. For this, the inflow dynamics state equations can be written by extending Peters-He's finite state rotor inflow formulation (Refs. [2] and [12])

$$
[M] \left\{ \begin{array}{c} \dot{\alpha}_n^{mc} \\ \dot{\alpha}_n^{ms} \end{array} \right\} + [L]^{-1} [V] \left\{ \begin{array}{c} \alpha_n^{mc} \\ \alpha_n^{ms} \end{array} \right\} = \left\{ \begin{array}{c} \tau_n^{mc} \\ \tau_n^{ms} \end{array} \right\} \quad (1)
$$

where α_n^{mc} and α_n^{ms} are the cosine and sine components of the inflow states, respectively. M is the apparent mass; L is the inflow influence coefficient matrix; V is the mass flow parameter matrix in a diagonal form; τ_n^{mc} and τ_n^{ms} are the inflow forcing functions related to rotor pressure sources. The inflow forcing functions can be computed from the blade circulatory lift (Refs. [2] and [12])

$$
\tau_n^{0c} = \frac{1}{4\pi} \sum_{q=1}^{N_b} [\int_0^1 L_q \phi_n^0(r) dr] cos(m\psi_q) \quad (2)
$$

$$
\tau_n^{mc} = \frac{1}{2\pi} \sum_{q=1}^{N_b} [\int_0^1 L_q \phi_n^m(r) dr] cos(m\psi_q) \quad (3)
$$

$$
\tau_n^{ms} = \frac{1}{2\pi} \sum_{q=1}^{N_b} [\int_0^R L_q \phi_n^m(r) dr] sin(m\psi_q) \quad (4)
$$

where L_q is the circulatory lift of the qth blade, N_b is the total number of blades, and $\phi_n^m(r)$ are the radial shape functions of the non-dimensional blade radial position, r, which can be computed as $\phi_n^m(r) = \frac{1}{\nu} \bar{P}_n^m(\nu)$ with $\nu = \sqrt{1-r^2}$ and $\bar{P}_n^m(\nu)$ is the normalized Legendre function of the first kind.

The **inflow output equations** consists of two parts. One is for the self-induced rotor inflow that can be directly generated once the inflow states are solved from Eq. 1. The other is the interference on other rotors and aerodynamic bodies/surfaces. The self-induced inflow output over each rotor plane is computed from an expansion in terms of both blade radial and rotor azimuthal variations

$$
w(r, \psi, t) = \sum_{m=0}^{\infty} \sum_{n=m+1,m+3,\cdots}^{\infty}
$$
$$
\phi_n^m(r)[\alpha_n^{mc}(t)cos(m\psi) + \alpha_n^{ms}(t)sin(m\psi)] \quad (5)
$$

Based on physical laws, the interference induced velocities at an arbitrary flow field point are a function of rotor source pressures (i.e., the inflow forcing functions) (Ref. [13]). With the rotor inflow states resolved from the rotor wake dynamics governed by Eq. 1, the interference velocity at an arbitrary flow field point can be formulated as a function of the outputs of the inflow state model with a time delay:

$$
\vec{w}_{intf}(x, y, z, t) = [H] \left\{ \begin{array}{c} \alpha_n^{mc}(t-\tau) \\ \alpha_n^{ms}(t-\tau) \end{array} \right\} \quad (6)
$$

where $\vec{w}_{intf}$ is the rotor induced interference velocity, which can have three velocity components; H is the interference output coefficient matrix; and τ is the time delay of the interference velocities with respect to the variation of the inflow states at the rotor. Both H and τ are functions of the geometrical location with respect to the interference source rotor as well as the flight conditions.

State-Space Inflow Model for Co-Axial Rotors

The general state-space model including the interference outputs (Eqs. 1 to 6) can be applied to a multiple rotor configuration. For each rotor, Eq. 1 governs the inflow states for the rotor while Eq. 6 forms the equation for the interference outputs. It is noticed that the inflow dynamic equation for each individual rotor of a multiple rotor system remains the same as Eq. 1. The coupling between the rotors comes from the inflow forcing functions (Eqs. 2 to 4 which include the effect of both self-induced and interference velocities (Eqs. 5 and 6). For a co-axial rotor system, the total rotor induced inflow for each rotor can be obtained from two parts: the self-induced inflow and the interference from the other rotor. Introducing the rotor index "1" and "2" for the upper and lower rotors, respectively, gives

$$w_1(r_1, \psi_1, t) = w_{11}^{self}(r_1, \psi_1, t) + w_{12}^{intf}(r_1, \psi_1, t) \quad (7)$$

$$w_2(r_2, \psi_2, t) = w_{22}^{self}(r_2, \psi_2, t) + w_{21}^{intf}(r_2, \psi_2, t) \quad (8)$$

where w_1 and w_2 are the total induced inflow of the upper and lower rotors, respectively, and w_{11}^{self} and w_{22}^{self} are the self induced rotor inflow of the upper and lower rotors, respectively. The self-induced inflow can be computed from the inflow states

$$
\begin{aligned}
w_{11}(r_1, \psi_1, t) &= \sum_{m,n}^{\infty} \phi_n^m(r_1)[\alpha_n^{mc1}(t)cos(m\psi_1) \\
&+ \alpha_n^{ms1}(t)sin(m\psi_1)] \quad (9) \\
w_{22}(r_2, \psi_2, t) &= \sum_{m,n}^{\infty} \phi_n^m(r_2)[\alpha_n^{mc2}(t)cos(m\psi_2) \\
&+ \alpha_n^{ms2}(t)sin(m\psi_2)] \quad (10)
\end{aligned}
$$

w_{12}^{intf} is the interference inflow at the upper rotor (indexed as "1") due to the lower rotor (indexed as "2") while w_{21}^{intf} is the interference inflow at the lower rotor due to the upper rotor. The interference inflow is computed from the interference Eq. 6 by taking the normal inflow that is the dominant component of the induced interference velocity for the mutual interference of a co-axial rotor system.

General Upper Rotor Inflow Equations

$$
\begin{aligned}
\begin{bmatrix} M_1 \end{bmatrix} \begin{Bmatrix} \dot{\alpha}_n^{mc1} \\ \dot{\alpha}_n^{ms1} \end{Bmatrix} &+ \begin{bmatrix} L_1 \end{bmatrix}^{-1} [V_1] \begin{Bmatrix} \alpha_n^{mc1} \\ \alpha_n^{ms1} \end{Bmatrix} \\
&= \begin{Bmatrix} \tau_n^{mc1} \\ \tau_n^{ms1} \end{Bmatrix} \quad (11) \\
w_{11}^{self}(r_1, \psi_1, t) &= \sum_{m,n} \phi_n^m(r_1)[\alpha_n^{mc}(t)cos(m\psi_1) \\
&+ \alpha_n^{ms}(t)sin(m\psi_1)] \quad (12) \\
w_{21}^{intf}(r_2, \psi_2, t) &= \begin{bmatrix} H_1 \end{bmatrix} \begin{Bmatrix} \alpha_n^{mc1}(t-\tau) \\ \alpha_n^{ms1}(t-\tau) \end{Bmatrix} \quad (13)
\end{aligned}
$$

General Lower Rotor Inflow Equations

$$
\begin{aligned}
\begin{bmatrix} M_2 \end{bmatrix} \begin{Bmatrix} \dot{\alpha}_n^{mc2} \\ \dot{\alpha}_n^{ms2} \end{Bmatrix} &+ \begin{bmatrix} L_2 \end{bmatrix}^{-1} [V_2] \begin{Bmatrix} \alpha_n^{mc2} \\ \alpha_n^{ms2} \end{Bmatrix} \\
&= \begin{Bmatrix} \tau_n^{mc2} \\ \tau_n^{ms2} \end{Bmatrix} \quad (14) \\
w_{22}^{self}(r_2, \psi_2, t) &= \sum_{m,n} \phi_n^m(r_2)[\alpha_n^{mc2}(t)cos(m\psi_2) \\
&+ \alpha_n^{ms2}(t)sin(m\psi_2)] \quad (15) \\
w_{12}^{intf}(r_1, \psi_1, t) &= \begin{bmatrix} H_2 \end{bmatrix} \begin{Bmatrix} \alpha_n^{mc2}(t-\tau) \\ \alpha_n^{ms2}(t-\tau) \end{Bmatrix} \quad (16)
\end{aligned}
$$

Induced Inflow Model Identification Method

The state-space rotor inflow model as formulated is derived by applying a numerical identification technique using the inflow response data from viscous VPM simulation. The model parameter identification method consists of two aspects: the generation of the inflow state response data from the VPM rotor wake excitation and the identification of the model parameters from the data using CIFER®. VPM simulation is first performed to generate inflow response data. To accomplish this, the blade bound circulation is prescribed in terms of a basic set of blade circulatory lifts (Refs. [5], [6], and [14]). For each prescribed inflow forcing function, a VPM simulation is performed to compute the induced inflow response over rotor planes and over the aerodynamic surfaces where the rotor wake interference are of interest. The distribution of the VPM induced inflow over the rotor planes are then further processed into the inflow states for the state-space inflow model parameter identification. The details regarding the inflow forcing

function formulation and the inflow state calculation from the inflow response data are described next.

Viscous Vortex Particle Method

The viscous Vortex Particle Method (VPM) (Refs. [7] and [8]) is used to carry out the numerical simulation to generate induced inflow perturbational data in response to the excitation of the inflow forcing functions. The inflow data are then used to extract the inflow model as formulated (Eqn. 1). VPM solves for the vorticity field directly from the vorticity-velocity form of the incompressible Navier-Stokes (N-S) equations using a Lagrangian formulation. The vorticity-velocity form with a Lagrangian description is a natural way of solving vorticity dominated flows due to the fact that it only needs to be applied to regions with vorticity and does not require any grid generation effort. In implementation, the entire vorticity field of the rotor wake is discretized into a set of N vector-valued vortex particles with distributed vorticity as

$$\vec{\omega}(\vec{x}, t) = \sum_{i=1}^{N} \xi_\sigma(\vec{x} - \vec{x}_i)\vec{\alpha}_i \quad (17)$$

where $\vec{\omega}$ is the vorticity strength carried by the vortex particle; $\vec{x}_i$ and $\vec{\alpha}_i$ are the position vector and the vector-valued total vorticity vector of particle i, respectively; and $\xi_\sigma(\vec{x})$ is the vorticity distribution function. In this research, a Super Gaussian distribution is used.

Based on incompressible N-S equations in vorticity-velocity form, the vortex particle dynamics (i.e., the unsteady change of both the vortex particle strength and location) are then governed by a convection-diffusion process as follows:

$$\frac{d\vec{\omega}}{dt} = \vec{\omega} \cdot \nabla \vec{u}_{tot} + \nu \Delta \vec{\omega} + \vec{\gamma}_{src} \quad (18)$$

$$\frac{d\vec{x}}{dt} = \vec{u}_{tot} = \vec{u}_\infty + \vec{u}_{vpm} + \vec{u}_{src} \quad (19)$$

Here, $\vec{\gamma}_{src}$ is the source vorticity originated from the aerodynamic surfaces and ν is the kinematic air viscosity. The dynamic motion of the vortex particles is driven by the total resultant air velocity ($\vec{u}_{tot}$), which is the vector sum of $\vec{u}_\infty$ (the free stream velocity), $\vec{u}_{vpm}$ (the VPM wake induced velocity), and $\vec{u}_{src}$ (the aerodynamic source induced velocity). In this development, the VPM rotor wake model is coupled with a lifting line based blade element model for vorticity source generation, which is directly related to blade bound circulation as

$$\vec{\gamma}_{src} = -\frac{d\vec{\Gamma}_b}{dt} + \vec{v}_b \nabla \cdot \vec{\Gamma}_b \quad (20)$$

where the first term is the shed vorticity and the second term is the trailed vorticity from each of the blade/wing segments with $\vec{v}_b$ as the resultant air velocity relative to the blade segment.

Prescribed Inflow Forcing Functions

Numerical VPM simulation is performed to generate inflow variation data for extracting the finite-state model parameters. To accomplish this, the inflow forcing function must be first prescribed. From the lifting line airloads solution, the blade bound circulation can be computed using the Kutta-Joukowski Theorem

$$\vec{L}_q = \rho \, \vec{v}_b \times \vec{\Gamma}_b \quad (21)$$

where $\vec{L}_q$ is the aero-segment lift, ρ is the air density, and $\vec{v}_b$ is the local segment air velocity.

To derive the inflow model parameters (i.e., both the apparent mass and inflow influence coefficients) from the VPM simulation, the blade bound circulation is prescribed in terms of a fundamental set of blade lifts. To simplify, the desired blade circulatory lift distribution can be selected as those that result in a linearly independent set of inflow forcing functions:

$$L_{nq}^{mc} = \frac{2\pi}{N_b} r\sqrt{1 - r^2}\phi_n^m(r)cos(m\psi_q) \quad (22)$$

$$L_{nq}^{ms} = \frac{2\pi}{N_b} r\sqrt{1 - r^2}\phi_n^m(r)sin(m\psi_q) \quad (23)$$

For a 3-state inflow model, the fundamental blade circulatory lift variation can be directly related to the variation of the overall rotor thrust, pitch moment, and roll moment. They can be written as follows:

$$L_{1q}^{0c} = \frac{2\pi}{N_b} r\sqrt{3(1 - r^2)} \quad (24)$$

$$L_{2q}^{1c} = \frac{2\pi}{N_b} r^2 \sqrt{\frac{15}{2}} \sqrt{(1 - r^2)}cos(\psi_q) \quad (25)$$

$$L_{2q}^{1s} = \frac{2\pi}{N_b} r^2 \sqrt{\frac{15}{2}} \sqrt{(1 - r^2)}sin(\psi_q) \quad (26)$$

where L_{1q}^{0c} is the first basic inflow forcing function related to the rotor thrust change, L_{2q}^{1c} is the second basic inflow forcing function related to the rotor pitch moment, and L_{2q}^{1c} is the third basic inflow forcing function related to the rotor roll moment. For the VPM rotor wake simulation, a blade bound circulation is prescribed, which can be computed via Eq. 21 and using Eqs. 24, 25, and 26. Figure 1 illustrates three inflow states and the corresponding blade bound circulation distribution for the first and second basic inflow forcing functions.

Induced Inflow States Extraction

The induced velocity response due to each rotor can then be computed through VPM simulation with the prescribed blade circulation. Let $w(r,\psi,t)$ (Eq. 5) be the perturbation induced inflow associated with a fundamental blade loading, which is obtained by the VPM wake simulation. The change of the expansion coefficients of the inflow distribution over the rotor (i.e., the inflow states, as expressed in Eq. 5), can then be computed as

$$\alpha_n^{0c} = \frac{1}{2\pi}\int_o^{2\pi}\int_0^1 [r\bar{P}_n^o(\nu)\,w(r,\psi,t)]drd\psi \quad (27)$$

$$\alpha_n^{mc} = \frac{1}{\pi}\int_o^{2\pi}\int_0^1 [r\bar{P}_n^m(\nu)cos(m\psi)w(r,\psi,t)]drd\psi \quad (28)$$

$$\alpha_n^{ms} = \frac{1}{\pi}\int_o^{2\pi}\int_0^1 [r\bar{P}_n^m(\nu)sin(m\psi)w(r,\psi,t)]drd\psi \quad (29)$$

where $\bar{P}_n^m$ are the normalized associated Legendre functions of the first kind that come from one of the general solutions of the potential flow equation for a rotor plane. The above inflow state calculation is based on Peters-He's inflow expansion formulation that has displayed good convergence characteristics over the rotor plane (Ref. [12]). Conventional 3-state inflow equation, which governs the inflow dynamics of the uniform, fore-aft linear first harmonic, and lateral linear harmonic variation, is a subset of the above expansion.

Rotor Interference Calculation

The rotor interference velocities on aerodynamic surfaces or bodies, such as the horizontal stabilator, vertical fin, fuselage, etc., are computed using the output equations with respect to the rotor inflow states as formulated in Eq. 6. In implementation, the numerical output matrix is extracted from the VPM simulation. To this end, the interference velocities at a given flow field point can be expanded using ellipsoidal coordinates as adopted in the original Peters-He finite-state inflow model formulation:

$$\vec{w}_{intf}^e(x,y,z,t) = \sum_{m,n} \vec{k}_n^{mc}S_n^{mc}(\nu,\eta,\Psi)\alpha_n^{mc}(t)$$
$$+ \ \vec{k}_n^{ms}S_n^{ms}(\nu,\eta,\Psi)\alpha_n^{ms}(t) \quad (30)$$

where $S_n^{mc}(\nu,\eta,\Psi)$ and $S_n^{ms}(\nu,\eta,\Psi)$ are the spatial interference expansion functions. In implementation, the interference velocities are divided into steady state and time perturbational components. The steady state component is computed using $\bar{\vec{k}}_n^{mc}$ and $\bar{\vec{k}}_n^{ms}$ as the fitting coefficients to match the interference velocities

with the VPM prediction for the steady state value. The time varying part of the interference is extracted from frequency analysis (CIFER®), which results in a gain, $\vec{k}$, and a time delay, $\vec{\tau}$. Both $\vec{k}$ and $\vec{\tau}$ are three-element vectors corresponding to the three interference velocity components of the interference velocity ($\vec{w}_{intf}$). The time delay reflects the time lag between the interference outputs and the rotor inflow states, which gives the final interference velocities as

$$\vec{w}_{intf}(x,y,z,t) = \left\{ \ S_n^{mc}(\nu,\eta,\Psi) \ \ S_n^{ms}(\nu,\eta,\Psi) \ \right\}$$
$$\left(\left\{\begin{array}{l}\vec{k}_n^{mc}\,\bar{\alpha}_n^{mc}\\\vec{k}_n^{ms}\,\bar{\alpha}_n^{ms}\end{array}\right\} \ + \ \left\{\begin{array}{l}\vec{k}\,\delta\alpha_n^{mc}(t-\vec{\tau})\\\vec{k}\,\delta\alpha_n^{ms}(t-\vec{\tau})\end{array}\right\}\right) \quad (31)$$

where $\bar{\alpha}_n^{mc}$ and $\bar{\alpha}_n^{ms}$ are the steady state inflow states and $\delta\alpha_n^{mc}$ and $\delta\alpha_n^{ms}$ are the time varying part of the inflow states.

Model Parameter Identification

A system identification tool based on a comprehensive frequency response approach (CIFER®, Ref. [9]) is the primary method used in this research. In implementation, a frequency sweep of each inflow forcing function is applied. The inflow state response corresponding to each of the inflow forcing functions computed from the VPM frequency sweep is then input to the CIFER® to extract the inflow model coefficient matrices. The detailed procedure for systematically extracting the inflow model parameters using the system identification method is summarized as follows

- Prescribe the blade bound circulation for each basic circulatory lift distribution.

- Run VPM simulation with the frequency sweep input of basic blade bound circulation one at a time.

- Collect the induced inflow distribution for both the self-induced and interference on other rotor and aerodynamic surfaces at each time instant.

- Compute the induced inflow states from the inflow distribution time history data as generated from the VPM simulation.

- Use CIFER® to compute the frequency responses and identify transfer functions and a state space inflow model.

- Apply CIFER® to identify the time delay between the VPM computed interference and the interpreted interference from the rotor inflow states.

Results and Discussion

The inflow model identification methodology was first tested with a single main rotor (UH-60A, Ref. [15]) and a general co-axial rotor system based on Harrington's rotor I configuration (Ref. [16]). The inflow model parameter identification method was tested and evaluated in both hover and forward flight for three fundamental rotor inflow forcing functions corresponding to the rotor thrust, rotor pitch, and rotor roll moment, respectively.

Single Rotor Test and Evaluation

A frequency response analysis was first performed to investigate the inflow model parameter identification method for single rotor configuration. Fundamental rotor inflow forcing functions corresponding to the blade circulation as related to the change in thrust and moment were applied. The VPM simulation with the prescribed basic circulatory lift distribution was first performed to reach a steady state and then a perturbation using a sinusoidal frequency sweep from the steady state was applied. In the frequency response test, the blade bound circulation was prescribed for a basic circulatory lift distribution corresponding to the thrust and moment variation. At each instant of the sweep run, the rotor induced inflow was sampled over the rotor plane for 30 radial segments and 48 azimuthal locations. The induced inflow distribution data thus collected were then used to compute the induced inflow states using Eqs. 27 to 29. The CIFER® frequency analysis and model identification tool (Ref. [9]) was used to identify the model parameters using the time inflow state history data generated from the VPM frequency sweep simulation with respect to the inflow forcing function as specified for the VPM tests.

Frequency Response in Hover For the frequency sweep cases simulated in hover, the starting and ending frequencies are 0.05 and 4.5 Hz, respectively. A range of perturbation magnitudes (from 5% to 20%) was investigated. The VPM simulation for each case was run for 90 seconds. Figure 2 shows the rotor wake iso-vorticity surface corresponding to the rotor thrust and pitch moment perturbation in hover, respectively. For the thrust perturbation, the rotor wake displays the typical characteristics of a hovering rotor. This includes the near wake contraction, the far wake pairing and diffusion, etc.. It is interesting to note that there is little wake contraction for the pitch moment perturbation because the overall total lift is nearly zero for the case of pitch moment perturbation.

Figure 3 displays the rotor inflow states excited from the thrust based inflow forcing function (τ_1^0) sweep tests. As expected, with the excitation of the thrust based inflow forcing function, the uniform inflow state dominates the response while the response of other two first harmonic states (both cosine and sine components) are minimal. Figure 4 displays the rotor inflow states excited from the pitch moment based inflow forcing function for the frequency sweep test. As shown, with the excitation of the pitch moment based inflow forcing function (τ_2^{1c}), the cosine cyclic inflow state (α_2^{1c}) dominates the response while the response of other two inflow states (uniform, α_1^{0c}, and sine inflow state, α_2^{1s}) are minor.

Table 1 summarizes the inflow model parameters for both uniform inflow and the cosine cyclic inflow states derived from the frequency response computed by CIFER®. For comparison, the model parameters were converted to Peters-He's format in terms of apparent mass and inflow influence coefficients. For each fit, CIFER® outputs a fitting cost to indicate the accuracy. A cost of less than 100 is considered to be a good fit (Ref. [9]). For this test, the fitting frequency range was from 0.06 to 3.2 Hz. As shown in the table, for a cost less than 100, the uniform inflow model derived from CIFER® identification has a small time delay of 39.6 ms. For comparison, the inflow model parameters were converted to Peters-He's format in terms of the apparent mass coefficients (M_{11} and M_{22}) and inflow influence coefficient (L_{11} and L_{22}). As shown, the derived inflow model parameters closely correlate with the original Peters-He finite-state model for both uniform and cyclic inflow states.

To evaluate, a Bode plot of the uniform inflow state in response to the thrust based forcing function excitation is shown in Fig. 5. The solid black line represents the inflow state variation from the raw VPM simulation data. The dash and dash-dot lines are CIFER® identified models with and without time delay, respectively. The blue solid line is the Peters-He's model. The model with a cost of 126 (dash-line) closely matches the Peters-He's model while the model with a time delay at a fitting cost of 55 (dash-dot line) moves closer toward the VPM raw state variation.

State-Space Inflow Model in Hover The frequency responses of the inflow states were used as inputs to CIFER® to identify a state-space inflow model in hover. Using CIFER®, the model parameters can be computed and the state-space inflow model in terms of

Table 1: Inflow Model Parameters (Hover)

	M_{11}	L_{11}	Time Delay	Cost
Peters-He	0.6366	0.7572	0	
VPM	0.6507	0.7522	39.6 ms	55
VPM	0.6507	0.7522	0	126
	M_{22}	L_{22}	Time Delay	Cost
Peters-He	0.4244	0.6250	0	
VPM	0.5500	0.5354	0	62

Table 2: State-Space Model Parameters as Identified in Hover

Element	Value	Cramer-Rao (%)
$\hat{m}_{11}$	0.0481	8.8
$\hat{m}_{22}$	0.0634	5.5
$\hat{m}_{33}$	0.0634	5.5
$\hat{m}_{32}$	0.0234	10
$\hat{m}_{23}$	0.0234	10
f_{11}	0.2970	4.7
f_{22}	0.3470	3.7
f_{33}	0.3470	3.7
f_{23}	0.0880	8.4
f_{32}	0.0880	8.4

direct CIFER®output was obtained as follows

$$
\begin{bmatrix} \hat{m}_{11} & 0 & 0 \\ 0 & \hat{m}_{22} & \hat{m}_{23} \\ 0 & \hat{m}_{32} & \hat{m}_{33} \end{bmatrix} \begin{Bmatrix} \dot{\alpha}_1^{0c} \\ \dot{\alpha}_2^{1c} \\ \dot{\alpha}_2^{1s} \end{Bmatrix} +
$$
$$
\begin{bmatrix} f_{11} & 0 & 0 \\ 0 & f_{22} & f_{23} \\ 0 & f_{32} & f_{33} \end{bmatrix} \begin{Bmatrix} \alpha_1^{0c} \\ \alpha_2^{1c} \\ \alpha_2^{1s} \end{Bmatrix} = \begin{Bmatrix} \tau_1^{0c} \\ \tau_2^{1c} \\ \tau_2^{1s} \end{Bmatrix} \quad (32)
$$

Table 2 lists the state-space model parameters extracted from CIFER®. It is noted that these are the inflow model parameters as identified that are not yet in general apparent mass and inflow influence coefficient format. For model accuracy assessment, the Cramer-Rao (CR) bound number as identified are also included in the table. The accuracy is considered to be satisfactory if the CR number is less than 10% (Ref. [9]). For further evaluation, the state-space model parameters are converted to the format of Pitt-Peters (Ref. [1]) in terms of inflow ($\bar{M}_{ij}$) and ($\bar{L}_{ij}$) as defined. The comparison between the identified model from VPM and the Pitt-Peters model parameters is shown in Table 3. The results using University of Maryland free wake (denoted as MFW) and Technion free wake (denoted as RFW) (Ref. [5]), respectively are also presented for comparison. Overall, the VPM extracted model parameters are compatible with Pitt-Peters' and the results from MFW and RFW. It is noticed that VPM shows larger $\bar{M}_{22}/\bar{M}_{33}$ than Pitt-Peters, but the $\bar{M}_{22}/\bar{M}_{33}$ from VPM is similar to what was obtained from MFW.

Table 3: Comparison with Pitt-Peters/MFW/RFW Model Parameters (Hover)

Element	VPM	Pitt-Peters	MFW	RFW
$\bar{M}_{11}$	0.0323	0.0312	0.0377	0.0312
$\bar{M}_{22}$	0.0085	0.0043	0.0080	0.0037
$\bar{M}_{33}$	0.0085	0.0043	0.0080	0.0037
$\bar{L}_{11}$	0.1980	0.2140	0.1920	0.1500
$\bar{L}_{22}$	0.0463	0.0500	0.0859	0.0547
$\bar{L}_{33}$	0.0463	0.0500	0.0825	0.0488

Frequency Response of Rotor Flapping in Hover
The inflow model extracted was evaluated by looking at the rotor coning response to a collective sweep. This was done by integrating the extracted inflow model with FLIGHTLAB®. A UH-60A rotor model was then used that includes the blade flapping dynamics and the finite-state inflow dynamics with the model parameters identified from CIFER® as described in the previous section. The collective frequency sweep tests were performed using three inflow models: VPM,

Peters-He, and the inflow model identified from the VPM-generated rotor inflow data via CIFER®. The frequency response of the rotor coning to the collective sweep was evaluated using CIFER® and the results are presented in Fig. 6. As shown, the identified inflow model agrees with the response of the Peters-He model and the direct VPM simulation. The comparison with flight test data (Ref. [5]) was also presented. In general, it shows a reasonable correlation except in the low frequency region where the body dynamics dominate. The prediction of the three models all deviate from the flight test there since none of the three simulations includes the body dynamics. Rotor flapping response to a cyclic pitch frequency sweep was also investigated. The rotor dynamic data in response to a frequency sweep of the longitudinal cyclic input were collected with the similar inflow models: VPM, Peters-He, and the identified state-space inflow model The corresponding frequency response of the rotor flapping to the frequency sweep is shown in Fig. 7. As shown, the identified model agrees with the response of the Peters-He model and closely correlates with the VPM simulation as well.

Validation of Time Response of Rotor Thrust/Flapping/Inflow in Hover The identified model was integrated with FLIGHTLAB® as a user-defined rotor inflow modeling component. The inflow dynamics model was then used in the FLIGHTLAB® simulation environment for further validation of the time response of the rotor transient flapping and inflow dynamics and the resulting thrust change in response to a step ramp-up of the collective pitch. The testing case simulated was a study of the rotor wake dynamics during a rapid increase in the collective pitch control. The validation study investigated the rotor inflow dynamics, the blade flapping, and the rotor thrust responses for a three-bladed articulated rotor in hover. The unsteady inflow, the blade flapping, and the thrust variations were measured for different rotor collective ramp inputs (Ref. [17]). For the inflow model evaluation, the rotor responses to two different increases of rotor collective pitch profiles were simulated.

The first simulation conducted was for the rotor step collective changes from 0 to 12 deg at a ramp-up rate of 200 deg/sec. Figures 8 to 10 show the transient response of the rotor inflow, rotor flapping, and rotor thrust coefficient in response to the 12 deg ramp-up collective input. The predicted response using the identified inflow model closely matches the measured rotor thrust changes in both transient dynamics and steady state. The prediction also shows a good agreement with measured rotor flapping except an under-predicted overshoot magnitude for this case. It is interesting to note that the VPM inflow dynamics displayed an overshoot of a second order dynamic system, a characteristic of its Navier-Stokes formulation which includes the effect of air viscosity, etc. The identified first order inflow dynamic model does capture the primary trend of the inflow dynamics and the prediction shows a good overall match in the resulting rotor flapping and thrust change as well. Finally, the inflow model time delay as identified from CIFER® was integrated in the simulation. Inclusion of the inflow time delay effect shows an improved inflow dynamic ramp-up as compared to the VPM and the measured data, although the change is fairly minor. It is interesting to also see that the time-delay matters even less for the coning and thrust response.

The second simulation test conducted was for the rotor collective changes from 0 to 12 deg at a lower rate (48 deg/sec). Figures 11 to 13 show the transient response of the rotor inflow, the rotor flapping, and the rotor thrust coefficient. Similar to the previous fast pull-up case (200 deg/sec), the predicted response using the identified inflow model closely correlates with the measured rotor inflow, thrust, and flapping changes in both transient dynamics and steady state. A similar minor improvement of the inflow response prediction was also exhibited by including the time delay as identified from CIFER®.

Frequency Response in Forward Flight Analysis of a single rotor in forward flight was conducted at a forward speed of 80 kts. Three sine-sweep simulations with VPM were run for the thrust (τ_1^{0c}), pitch moment (τ_2^{1c}), and roll moment (τ_2^{1s}) based inflow forcing function, respectively. The frequency sweep for each VPM simulation was run for 90 seconds with a sweep range from 0.05 to 8.0 Hz. The response of the inflow states to the excitation of each inflow forcing function was collected, which were then inputted into CIFER® for frequency response analysis. The CIFER® was first applied to extract the best fit SISO transfer functions. In total, nine transfer functions were obtained. The fitting cost for all the transfer functions is less than 40, which indicates an excellent fit.

Figure 14 shows the variation (perturbation in percent) of the thrust based inflow forcing function (τ_1^{0c}). A snapshot of the rotor wake corresponding to the τ_1^{0c} excitation is shown in Fig. 15. At 80 kts forward flight speed, the rotor wake is relatively flat. The helical wake geometry and the roll-up of tip vortices can be well observed. Figure 16 shows the time variation of the rotor inflow states resulting from the (τ_1^{0c}) excitation. As shown, both the uniform and fore-aft inflow (1st cosine harmonic) states dominate the response. The fore-aft cosine harmonic inflow state represents the induced inflow distribution associated with the rotor thrust change due to the rotor wake skewing in forward flight. There is also a sine harmonic inflow state resulting from the τ_1^{0c} excitation, but its magnitude is smaller than the other two inflow states. Figure 17 shows the comparison of state-space model, transfer function fit, and the VPM simulation data. A close correlation was seen. Figure 18 shows the frequency response of the cosine cyclic inflow state response from the same τ_1^{0c} excitation and comparison of state-space model, transfer function fit, and the VPM simulation data as well. Similar close correlation was seen. The inflow state response from the pitch moment based inflow forcing function (τ_2^{1c}) excitation is shown in Fig. 19. All inflow states (uniform, cosine harmonic, and sine harmonic) were excited. Figure 20 presents the corresponding frequency response of the inflow states. The frequency response of the inflow states from the state-space model was also verified with VPM response data and a close correlation was obtained. The inflow state response from the roll moment based inflow forcing function (τ_2^{1s}) excitation is shown in Fig. 21. The cosine and sine harmonic inflow states were coupled while the response of the

uniform inflow state is much smaller. Figure 22 presents the corresponding frequency response of the inflow states from the τ_2^{1s} excitation.

State-Space Inflow Model in Forward Flight   Using physical inflow state formulation (i.e., the uniform and the first cosine and sine harmonic) and applying CIFER®, a 3-state inflow model in forward flight (80 knots) was extracted from VPM simulation data as follows

$$
\begin{bmatrix} \hat{m}_{11} & 0 & 0 \\ 0 & \hat{m}_{22} & \\ 0 & 0 & \hat{m}_{33} \end{bmatrix} \begin{Bmatrix} \dot{\alpha}_1^{0c} \\ \dot{\alpha}_2^{1c} \\ \dot{\alpha}_2^{1s} \end{Bmatrix} + \\
\begin{bmatrix} f_{11} & f_{12} & 0 \\ f_{21} & f_{22} & 0 \\ 0 & 0 & f_{33} \end{bmatrix} \begin{Bmatrix} \alpha_1^{0c} \\ \alpha_2^{1c} \\ \alpha_2^{1s} \end{Bmatrix} = \begin{Bmatrix} \tau_1^{0c} \\ \tau_2^{1c} \\ \tau_2^{1s} \end{Bmatrix} \quad (33)
$$

The corresponding model parameters identified are listed in Table 4.

Table 4: State-Space Model Parameters (80 Knots)

Element	Value	Cramer-Rao (%)
$\hat{m}_{11}$	0.0915	3.4
$\hat{m}_{22}$	0.1059	5.8
$\hat{m}_{33}$	0.0631	8.5
f_{11}	0.0796	9.8
f_{21}	-2.5081	3.4
f_{12}	0.5043	4.1
f_{22}	1.4435	4.1
f_{33}	0.6476	4.2

Interference Evaluation   The rotor interference calculation formulated as the outputs from a state-space inflow model (Eq. 6) was tested and evaluated using a VPM simulation of a UH-60A rotor. For the study, the VPM simulation for a thrust based sweep was performed at 80 kts forward flight speed. The rotor induced velocities were investigated at five off-rotor flow field points: fuselage, tail boom, vertical fin, and left and right horizontal surfaces. Figure 23 illustrates the location of the five selected flow field points for the interference investigation.

The interference velocity outputs generated from the VPM simulation can be organized in two parts, i.e., the time-averaged and time-varying about the averaged. For a rotorcraft configuration given, the locations of interference velocity of interest with respect to rotor, such as a horizontal surface, are known. Therefore, it is relatively straightforward to compute the time-averaged via a table look-up. But, the dynamics of the interference need to be identified via parameter identification technique. It was found from this study that a combined gain and time delay are sufficient to capture the unsteady interference due to the rotor disturbance.

Table 5: Off-Rotor Interference Calculation

	gain	delay (ms)
Fuselage	1.0554	0.0
Tail Boom	1.3400	29.9
V-fin	0.9317	113.8
Left h-stab	1.0115	106.9
Right h-stab	0.6957	86.0

The fitting coefficients computed for the five flow field points from the steady state VPM simulation data were used to generate the estimated rotor interference using Eq. 30. As expressed in the equation, the estimated rotor interference velocity is essentially a linear combination of the rotor inflow states. A time delay and gain of the estimated interference velocities can be extracted using the CIFER® tool (Ref. [9]). To do this, the estimated interference velocity component at a given point, one at a time, was used as an input and the corresponding VPM predicted time variation of the interference at the same point was output. Both the oscillation magnitude gain and time delay parameters were then computed by CIFER®.

Figure 24 shows the time variation of the estimated and the VPM prediction of the downwash at the fuselage (Point 1). The estimation shows a close correlation with the VPM prediction. The corresponding frequency response is displayed in Fig. 25. Both the gain and the time delay extracted from the CIFER® analysis are listed in Table 5. As expected, there is no time delay of the rotor interference at fuselage sampling point since the fuselage point is very close to the rotor. Figures. 26 and 27 show both the time and frequency variation of the estimated and the VPM prediction of the downwash at vertical fin (Point 3), respectively. The estimated downwash is correlates closely with the VPM prediction. At the vertical fin, the interference downwash incurs a time delay of 113.8 ms. Figures. 28 and 29 show both the time and frequency variation of the estimated and the VPM prediction of the downwash at left horizontal stabilator surface (Point 4), respectively. Good correlation can be seen for the estimated and the VPM predicted downwash. Similar good correlation was seen between the estimated interference downwash and the VPM prediction at the right horizontal stabilator surface

also. For the UH-60 class helicopter, the geometrical distance of the vertical fin and the horizontal stabilator is slightly greater than one rotor radius. At 80 kts of forward flight, a new vortex particle would take about 200 ms to travel the geometrical distance from the rotor to the horizontal stabilator. It is interesting to note that the interference wave transportation time is about half of that of geometrical travel. It is also observed from Table 5 that the downwash gain values vary with interference sampling points. The gain at tail boom point shows the highest value implying that the downwash oscillation there is the highest, which indicates that the tail boom sampling point is closer to the dominant part of rotor wake (Fig. 23).

Co-Axial Rotor Test and Evaluation

The inflow model identification method as outlined was applied to a coaxial rotor. The Harrington rotor system with configuration I was selected for this study. The two rotors of the coaxial system are identical. Each rotor comprises two untwisted blades with a radius of 12.5 ft. The root-cutout of each rotor is 21% of the rotor radius and the blades are linearly tapered. The rotational speed of each rotor is 37.52 rad/s. The inter-rotor vertical separation distance is 0.19R. The detailed specifications of this coaxial rotor system can be obtained from Ref. [16] The state-space inflow model was identified in hover for the coaxial rotor system. The methodology was also tested in forward flight. Based on the unified state-space rotor inflow model formulation (Eqns. 11 to 15), the induced velocity on each rotor comprises self-induced velocity and the interference induced velocity from the other rotor. The self-induced velocity is calculated from the inflow expansion coefficients or inflow states of the rotor to which the frequency sweep perturbation is applied. The interference induced velocity on the other rotor is calculated from the interference inflow expansion coefficients, which are derived from the inflow state solution of the interfering rotor.

Co-Axial Rotor Thrust Based Frequency Sweep Response in Hover For comparative studies, three simulation cases were tested. It includes (1) *baseline* single rotor frequency sweep; (2) the *upper rotor* frequency sweep; and (3) the *lower rotor frequency sweep*. For the baseline single rotor case, a basic blade circulation distribution corresponding a thrust forcing function was applied to a single rotor from the Harrington Rotor I system. The steady value of the forcing function was τ_1^0=0.005. Figure 30 shows a frequency sweep thrust forcing that was applied to the baseline rotor. The amplitude of the perturbation was 20% of the steady state forcing value and the frequencies were varied between 0.05 and 8 Hz. The

total duration of the frequency sweep was 90 sec. The same forcing τ_1^{01}=0.005 with a frequency sweep perturbation shown in Fig. 30 was applied to the upper rotor and the lower rotor of the coaxial system, respectively. For the upper rotor frequency sweep perturbation, the lower rotor was prescribed to a mean steady state value of τ_1^{02}=0.005, while for the lower rotor frequency sweep perturbation, the upper rotor forcing was prescribed to the similar mean value. Note that the second superscript used in τ_1^{01} and τ_1^{02} denotes the rotor to which the forcing has been applied (i.e., index "1" and "2" show forcing applied to the upper and the lower rotors, respectively). During the frequency sweep simulation, the velocities induced were sampled at both the rotor planes using 15 radial segments and 48 azimuthal locations. For the upper rotor frequency sweep, the velocities sampled on the upper rotor were used to calculate the upper rotor inflow states (α_1^{0c1}, α_2^{1c1}, α_2^{1s1}) and the velocities sampled on the lower rotor were used to calculate the lower rotor interference inflow expansion coefficients ($\tilde{\alpha}_1^{0c2}$, $\tilde{\alpha}_2^{1c2}$, $\tilde{\alpha}_2^{1s2}$). The time histories of the frequency sweep input (τ_1^{01}) and the upper rotor inflow states and lower rotor inflow expansion coefficients were analyzed in CIFER® to obtain their frequency responses and the lowest-order transfer functions that best represent the frequency responses. Similar process was applied for the lower rotor frequency sweep.

A comparison of the vorticity contours along the longitudinal plane passing through the rotor hub obtained during a steady thrust-based forcing and after the 90 sec frequency sweep simulations were applied to the upper and lower rotors is shown in Fig. 31. The top contour as shown is for the vorticity variation at the end of steady state before the frequency sweep perturbation starts. The middle contour is for the vorticity variation due to the upper rotor perturbation while the bottom contour is for the lower rotor perturbation. Both are the vorticity contours at the end of frequency sweep (i.e., time at 90 seconds) when the co-axial rotor wake was formed with the vortex particles accumulated from the overall wake development. It is noted that the wakes obtained from the upper and lower rotor frequency sweep simulations at t = 90 sec show different patterns, with the regions of vortex concentration into rings forming at different downstream distances, even though the perturbation becomes zero at 90 sec (see Fig. 30).

Figure 32 displays the time histories of the inflow states of the upper rotor (as shown in the upper plot) and the interference inflow expansion coefficients of the lower rotor (as shown in the lower plot) resulting from the upper rotor thrust excitation. It can be seen that the dominant response from the thrust excitation is the upper rotor uniform inflow state and the lower rotor

uniform interference expansion coefficient.

Figure 33 presents a comparison of the upper rotor uniform inflow state (α_1^{0c1}) and lower rotor uniform interference expansion coefficient ($\tilde{\alpha}_1^{0c2}$) obtained from the upper rotor thrust frequency sweep excitation (as shown in the upper plot) The figure also shows the uniform inflow state (α_1^{0c}) obtained from the baseline thrust frequency sweep excitation. The results show that the coupled wake system of the coaxial rotor induces about 27% higher inflow velocity on the lower rotor when compared to the upper rotor because of the impingement of the wake from the upper rotor on the lower rotor. When compared with the baseline rotor, the mean inflow on the upper and the lower rotors are about 20% and 52% higher than the baseline rotor because of the coupled effects of the coaxial rotor wake (as shown in the upper graph). Figure 33 also displays the perturbational time histories of the uniform inflow states/interference expansion coefficient about the steady state value (as shown in the lower graph) It is noticed that the perturbational magnitudes of both upper and lower rotor of the co-axial rotor system are less than that of baseline (the isolated single rotor). This is further confirmed in corresponding frequency response results.

Figure 34 shows the frequency responses of the baseline, upper, and lower rotor uniform inflow variations with respect to the thrust frequency sweep forcing were obtained using CIFER® . The results show that the perturbations in the upper and the lower rotor uniform inflows are 19.5% and 22% smaller when compared to that of the baseline rotor uniform inflow response, which suggests that the effect of thrust-based perturbations to the rotor wake response attenuate in the presence of two counter-spinning rotors. The lower rotor uniform inflow perturbations are about 3% higher in amplitude when compared to the upper rotor for the upper rotor thrust frequency sweep.

The resulting response of the lower rotor inflow state and the upper rotor interference inflow expansion coefficient as calculated by VPM for the lower rotor frequency sweep, along with the baseline inflow state variation, are shown in Fig. 35. The results show that, for the lower rotor frequency sweep, the resulting perturbations in the upper ($\tilde{\alpha}_1^{0c1}$) and lower (α_1^{0c2}) rotor uniform inflow responses are smaller when compared to the baseline rotor uniform inflow perturbations (α_1^{0c}). The frequency responses obtained from the lower rotor frequency sweep are shown in Fig. 36. The results show that the lower rotor frequency sweep produces 60% and 30% smaller uniform inflow perturbations on the upper and lower rotors, respectively, when compared to the baseline uniform inflow perturbations. Comparing the interference on the lower rotor due to the upper rotor

excitation (Fig. 34 with the interference on the upper rotor due to the lower rotor excitation (Fig. 36), the upper rotor excitation produces a larger disturbance on the lower rotor than the otherwise.

Co-Axial Rotor Pitch Moment Based Frequency Sweep Response in Hover Two VPM simulations were conducted with pitch moment based forcing distributions applied to the upper and lower rotors, respectively. In both of these simulations, a steady pitch moment forcing of $\tau_2^{1c1} = \tau_2^{1c2} = 0.0006$ was first applied to both the rotors and the steady-state wake of the coaxial system was obtained. The frequency sweep forcing as shown in Fig. 37 was then applied to the upper and lower rotors, one at a time, while the other rotor was maintained at the steady forcing. The duration of the simulations was 90 sec.

Upper rotor pitch moment forcing simulation:
The time histories of the inflow distribution on the upper and lower rotor planes from the upper rotor pitch moment forcing simulation in VPM were used to calculate the upper rotor inflow states (i.e., α_1^{0c1}, α_2^{1c1}, α_2^{1s1}) and the lower rotor interference inflow expansion coefficients (i.e., $\tilde{\alpha}_1^{0c2}$, $\tilde{\alpha}_2^{1c2}$, $\tilde{\alpha}_2^{1s2}$). Figure 38 shows the total upper rotor states and the lower rotor interference expansion coefficients as well as the perturbations about the mean values. The frequency responses of the upper and lower rotor inflow to the pitch moment excitation input are shown in Figs. 39 and 40, respectively. The results show that the magnitude of the frequency response of the upper rotor uniform inflow state (α_1^{0c1}) is much less than that of the cosine inflow state (α_2^{1c1}) (Fig. 39). Therefore, this response is neglected for the development of the coaxial rotor state-space inflow model in hover. Similarly, the uniform inflow interference expansion coefficient of the lower rotor ($\tilde{\alpha}_1^{0c2}$) is also ignored during the construction of the inflow model (Fig. 40).

Lower rotor pitch moment forcing simulation:
In this VPM simulation, the blade circulation over the lower rotor was prescribed by the pitch moment frequency sweep forcing as shown in Fig. 37, while the upper rotor blade circulation was prescribed according to the mean forcing of $\tau_2^{1c1} = 0.0006$. The resulting interference inflow expansion coefficients on the upper rotor (i.e., $\tilde{\alpha}_1^{0c1}$, $\tilde{\alpha}_2^{1c1}$, $\tilde{\alpha}_2^{1s1}$) and the lower rotor states (i.e., α_1^{0c2}, α_2^{1c2}, α_2^{1s2}) are shown in Fig. 41. The frequency responses of the upper interference inflow expansion coefficients to the pitch moment forcing input are shown in Figs. 42 and the response of the lower rotor inflow states are shown in Fig. 43. The inflow response similar to the previous pitch moment based excitation can be observed.

Coaxial Rotor State-Space Model in Hover
State-space inflow models were developed for the upper and lower rotors of the coaxial system in hover using the Single Input Multiple Output (SIMO) frequency responses to the thrust and pitch moment excitations as discussed in the previous section. Note that, in hover, the pitch and roll-moment excitations are identical because of the axi-symmetric flow field.

The state-space matrices are identified for each rotor of the coaxial system. These state-space matrices solve for the self-induced inflow states of each rotor, which are used to calculate the self-induced velocity on the rotor plane. The interference inflow expansion coefficients on the other rotor are calculated as outputs from the interfering rotor's inflow states. For example, the upper rotor inflow state equation solves for the upper rotor inflow states (α_1^{0c1}, α_2^{1c1}, α_2^{1s1}), and also provides lower rotor's interference inflow expansion coefficients ($\tilde{\alpha}_1^{0c2}$, $\tilde{\alpha}_2^{1c2}$, $\tilde{\alpha}_2^{1s2}$) as outputs.

For the upper and lower rotors, the SIMO analysis obtained from the thrust-based forcing showed that the uniform inflow state is the dominant response. SIMO frequency domain analysis of the pitch moment input showed that the cosine and sine states are coupled. The identified state-space model for the upper rotor was obtained as follows,

$$
\begin{bmatrix} 0.0432 & 0 & 0 \\ 0 & 0.0437 & 0.0088 \\ 0 & 0.0088 & 0.0437 \end{bmatrix} \begin{Bmatrix} \dot{\alpha}_1^{0c1} \\ \dot{\alpha}_2^{1c1} \\ \dot{\alpha}_2^{1s1} \end{Bmatrix} +
$$
$$
\begin{bmatrix} 0.3930 & 0 & 0 \\ 0 & 0.2780 & 0.0325 \\ 0 & 0.0325 & 0.2780 \end{bmatrix} \begin{Bmatrix} \alpha_1^{0c1} \\ \alpha_2^{1c1} \\ \alpha_2^{1s1} \end{Bmatrix} = \begin{Bmatrix} \tau_1^{0c1} \\ \tau_2^{1c1} \\ \tau_2^{1s1} \end{Bmatrix}
$$
$$(34)$$

The fitting cost cost was all less than 100 and the Cramer-Rao bounds of the identified state-space parameters of the upper rotor were all less than 10%. The interference inflow expansion coefficients of the lower rotor can be obtained from the upper rotor inflow states as:

$$
\begin{Bmatrix} \tilde{\alpha}_1^{0c2}(t) \\ \tilde{\alpha}_2^{1c2}(t) \\ \tilde{\alpha}_2^{1s2}(t) \end{Bmatrix} =
$$
$$
\begin{bmatrix} 1.2689 & 0 & 0 \\ 0 & 1.5821 & 0 \\ 0 & 0 & 1.5821 \end{bmatrix} \begin{Bmatrix} \alpha_1^{0c1}(0) \\ \alpha_2^{1c1}(0) \\ \alpha_2^{1s1}(0) \end{Bmatrix}
$$
$$
+ \begin{bmatrix} 1.0431 & 0 & 0 \\ 0 & 1.4424 & 0 \\ 0 & 0 & 1.4424 \end{bmatrix} \begin{Bmatrix} \alpha_1^{0c1}(t) \\ \alpha_2^{1c1}(t) \\ \alpha_2^{1s1}(t) \end{Bmatrix}
$$
$$(35)$$

The state-space model identified for the lower rotor inflow states was obtained as:

$$
\begin{bmatrix} 0.0383 & 0 & 0 \\ 0 & 0.0270 & 0 \\ 0 & 0 & 0.0270 \end{bmatrix} \begin{Bmatrix} \dot{\alpha}_1^{0c2} \\ \dot{\alpha}_2^{1c2} \\ \dot{\alpha}_2^{1s2} \end{Bmatrix}
$$
$$
+ \begin{bmatrix} 0.4579 & 0 & 0 \\ 0 & 0.5439 & 0.3160 \\ 0 & 0.3160 & 0.5439 \end{bmatrix} \begin{Bmatrix} \alpha_1^{0c2} \\ \alpha_2^{1c2} \\ \alpha_2^{1s2} \end{Bmatrix}
$$
$$
= \begin{Bmatrix} \tau_1^{0c2} \\ \tau_2^{1c2} \\ \tau_2^{1s2} \end{Bmatrix} (t - \boldsymbol{\tau}) \qquad (36)
$$

where the time delay matrix is identified as:

$$
\boldsymbol{\tau} = \begin{bmatrix} 0.02370 & 0 & 0 \\ 0 & 0.03840 & 0 \\ 0 & 0 & 0.03840 \end{bmatrix} \qquad (37)
$$

Notice that except the time delay element from the thrust excitation to the uniform inflow response, the Cramer-Rao bounds of the identified elements of the state-space matrix were all less than 20%.

The interference inflow expansion coefficients of the upper rotor due to the lower rotor inflow states was obtained as:

$$
\begin{Bmatrix} \tilde{\alpha}_1^{0c1}(t) \\ \tilde{\alpha}_2^{1c1}(t) \\ \tilde{\alpha}_2^{1s1}(t) \end{Bmatrix} =
$$
$$
\begin{bmatrix} 0.7881 & 0 & 0 \\ 0 & 0.6321 & 0 \\ 0 & 0 & 0.6321 \end{bmatrix} \begin{Bmatrix} \alpha_1^{0c2}(0) \\ \alpha_2^{1c2}(0) \\ \alpha_2^{1s2}(0) \end{Bmatrix} +
$$
$$
\begin{bmatrix} 0.5712 & 0 & 0 \\ 0 & 0.5430 & 0 \\ 0 & 0 & 0.5430 \end{bmatrix} \begin{Bmatrix} \alpha_1^{0c2}(t) \\ \alpha_2^{1c2}(t) \\ \alpha_2^{1s2}(t) \end{Bmatrix}
$$
$$(38)$$

Time Response Verification Tests The extracted 3-state inflow model for a coaxial system in hover was further evaluated in the time-domain. The time responses of the upper and lower rotor uniform inflow states and interference expansion coefficients to a step change in the thrust based forcing function were compared to the original VPM simulation. Figure 44 shows the upper rotor uniform inflow state and the lower rotor uniform interference inflow expansion coefficient obtained for a step ramp-up (0.5 sec) of the upper rotor thrust based inflow forcing function. The inflow response on both rotors from the 3-state model show good agreement with the transient inflow response from the VPM simulation.

Similarly, Fig. 45 shows the lower rotor uniform inflow state and the upper rotor uniform interference

inflow expansion coefficient obtained for a step ramp-up (0.5 sec) of the lower rotor thrust based inflow forcing function. The results show good agreement with the VPM transient response for the lower rotor inflow and a reasonable response for the upper-rotor inflow from the lower rotor thrust-based excitation.

Co-Axial Rotor in Forward Flight The coaxial rotor inflow model identification methodology was also tested in forward flight at 40 kts. The following sections discuss only the thrust-based frequency sweep forcing results. The results for the pitch and roll-moment forcing can be extracted in a similar way.

Upper Rotor Frequency Sweep Forcing:

A VPM simulation was conducted for the coaxial rotor system in forward flight at 40 kts. Both of the rotors of the coaxial system were subjected to a blade lift distribution corresponding to a thrust forcing $\tau_1^{01} = \tau_1^{02} = 0.005$. A steady VPM wake solution was first obtained. The thrust-based frequency sweep forcing distribution was then applied to the upper rotor blades. The perturbation of the forcing about the value of $\tau_1^{01} = 0.005$ is shown in Fig. 30.

Figure 46 shows the coaxial system steady wake at 40 kts. The helical nature and the roll-up of the wake can be observed. Figure 47 shows shows the time variation of the upper rotor inflow states (α_1^{0c1}, α_2^{1c1}, α_2^{1s1}) and the lower rotor inflow expansion coefficients ($\tilde{\alpha}_1^{0c2}$, $\tilde{\alpha}_2^{1c2}$, $\tilde{\alpha}_2^{1s2}$) resulting from τ_1^{01} excitation at 40 kts. The results show that the uniform and the fore-aft (cosine) inflow states and interference inflow expansion coefficients dominate the response while the sine harmonic response is much less. Figure 48 shows the inflow frequency responses due to the τ_1^{01} (thrust-based) excitation. The results show that, at lower frequencies, the upper rotor experiences about 16% higher amplitude perturbations in uniform inflow and 5% smaller amplitude oscillations in fore-to-aft inflow when compared to the lower rotor. In general, the results show that, unlike in hover, the inflow responses from both the rotors at 40 kts are similar in magnitude for the upper rotor thrust excitation.

Lower-Rotor Frequency Sweep Forcing:

The frequency response to the lower rotor thrust-based frequency sweep was performed in a similar way. First, a steady VPM wake was obtained for the case where both of the rotors of the coaxial system were subjected to the same thrust-based blade lift distribution. The thrust-based frequency sweep forcing variation, as shown in Fig. 30, was then applied to the lower rotor. Figure 49 shows the corresponding frequency responses. The results show that the lower rotor thrust excitation in 40 kt forward flight produces dominant responses in the uniform and the fore-aft

(first harmonic cosine) inflow components. The first sine harmonic response is at least an order magnitude smaller when compared to the uniform or the first cosine responses and can therefore be neglected. The effect of the lower rotor excitation is dominant on the lower rotor. At lower frequencies, the uniform inflow response on the upper rotor ($\tilde{\alpha}_1^{0c1}$) and the first cosine response ($\tilde{\alpha}_2^{1c1}$) are about 70% and 55% that of the respective responses on the lower rotor.

Summary and Conclusions

Future vertical lift configuration design considers advanced configurations that usually have multiple rotors (e.g., co-axial, tilt-rotor, quad-rotors), ducted fans, auxiliary wings, etc. Advances in rotor induced inflow simulation methods are needed to extend the current modeling capability beyond the conventional single main rotor configurations in order to effectively support the flight dynamics simulation and flight control system design and development for advanced rotorcraft configurations. This research aims to develop a state-space rotor inflow model to meet this need. The current research has resulted in the development of a unified state-space inflow formulation as well as the model parameter identification methodology. In summary, the research has accomplished

- A unified state-space rotor induced inflow formulation intended for flight dynamics and control analysis applications was formulated. The model thus derived is well suited for multiple rotor (e.g., co-axial) configurations.

- The methodology was developed using CIFER® to identify the inflow model parameter from first principle based VPM simulation data.

- The inflow model formulation and the corresponding model parameter identification method were first tested and evaluated for a single main rotor configuration in both hover and forward flight. The inflow models were validated with available measured data, including the comparison of the simulated response of the induced inflow, rotor flapping, and rotor thrust.

- The inflow model formulation and the corresponding model parameter identification method were also tested and evaluated for a co-axial rotor configuration in both hover and forward flight. A close correlation between the identified model and original VPM simulation response was obtained, which demonstrates the viability and accuracy of the model identification methodology for multiple rotor systems.

- It was demonstrated that a first order state-space inflow model as derived accurately captured the physical inflow dynamics and, hence, offers a good approximation for practical applications. Linear characteristics of inflow dynamics in the low frequency range of flight dynamics interest was demonstrated by high coherence of all frequency response cases as investigated.

Acknowledgment

References

[1] Pitt, D. and Peters, D. A., "Dynamic Inflow for Practical Applications," *Vertica*, Vol. 5, No. 1, 1981.

[2] Peters, D. A. and He, C., "Finite State Induced Flow Models Part II: Three Dimensional Rotor Disk," *Journal of Aircraft*, Vol. 32, No. 2, March-April 1995, pp. 323–333.

[3] Nowak, M., Prasad, J., and Peters, D., "Development of a Finite State Model for a Coaxial Rotor in Forward Flight," *American Helicopter Society 70th Annual Form*, Quebec, Canada, May 2014.

[4] Fegely, C., Juhasz, O., Hong, X., and Tischler, M., "Flight Dynamics and Control Modeling with System Identification Validation of the Sikorsky X2 Technology Demonstrator," *American Helicopter Society 72nd Annual Form*, West Palm Beach, FL, May 2016.

[5] Rand, O., Khromov, V., Hersey, S., Celi, R., Juhasz, O., and Tischler, M., "Linear Inflow Model Extraction from High-Fidelity Aerodynamic Models for Flight Dynamics Applications," *American Helicopter Society 71st Annual Form*, Virginia Beach, VA, May 2015.

[6] Rand, O. and Khromov, V., "Free-Wake Based Dynamic Inflow Model for Hover, Forward and Maneuvering Flight," *American Helicopter Society 72nd Annual Form*, West Palm Beach, FL, May 2016.

[7] He, C. and Zhao, J., "Modeling Rotor Wake Dynamics with Viscous Vortex Particle Method," *AIAA Journal*, Vol. 47, No. 4, April 2009.

[8] Zhao, J. and He, C., "A Viscous Vortex Particle Model for Rotor Wake and Interference Analysis," *Journal of the American Helicopter Society*, Vol. 55, No. 1, January 2010.

[9] Tischler, M. B. and Remple, R., *Aircraft and Rotorcraft System Identificaiton*, AIAA Education, 2nd Revised Edition, 2013.

[10] He, C. and Zhao, J., "High Fidelity simulaiton of Tiltrotor Aerodynamic Interference," *Proceedings of 68th Annual Forum of the American Helicopter Society*, Fort Worth, TX, May 2012.

[11] He, C. and Rajmohan, N., "Modeling the Aerodynamic Interaction of Multiple Rotor Vehicles and Compound Rotorcraft with Viscous Vortex Particle Method," *Proceedings of 72nd Annual Forum of the American Helicopter Society*, West Palm Beach, May 2016.

[12] He, C., *Development and Application of Generalized Dynamic Wake Theory for Lifting Rotors*, Ph.D. thesis, School of Aerospace Engineering, Georgia Institute of Technology, July 1989.

[13] He, C., "Finite State Dynamic Wake Interference Modeling for Rotorcraft Simulation," *Proceedings of 53rd Annual Forum of the American Helicopter Society*, Virginia Beach, VA, April 1997.

[14] He, C. and Zhao, J., "A Real Time Finite State Induced Flow Model Augmented with High Fidelity Viscous Vortex Particle Simulation," *Proceedings of 64th Annual Forum of the American Helicopter Society*, Montreal, Canada, April 2008.

[15] Howlett, J., "UH-60A Black Hawk Engineering Simulation Program: Vol I: Mathematical Model," NASA CR 166309, December 1981.

[16] Harrington, R., "Full-Scale-Tunnel Investigation of the Static Thrust Performance of a Coaxial Helicopter Rotor," NACA TN 2318, 1951.

[17] Carpenter, P. and Fridovich, B., "Effect of a Rapid Blade-Pitch Increase on the Thrust and Induced-Velocity Response of a Full-Scale Helicopter Rotor," NACA TN 3044, 1953.

Three Inflow States

Blade bound circulation
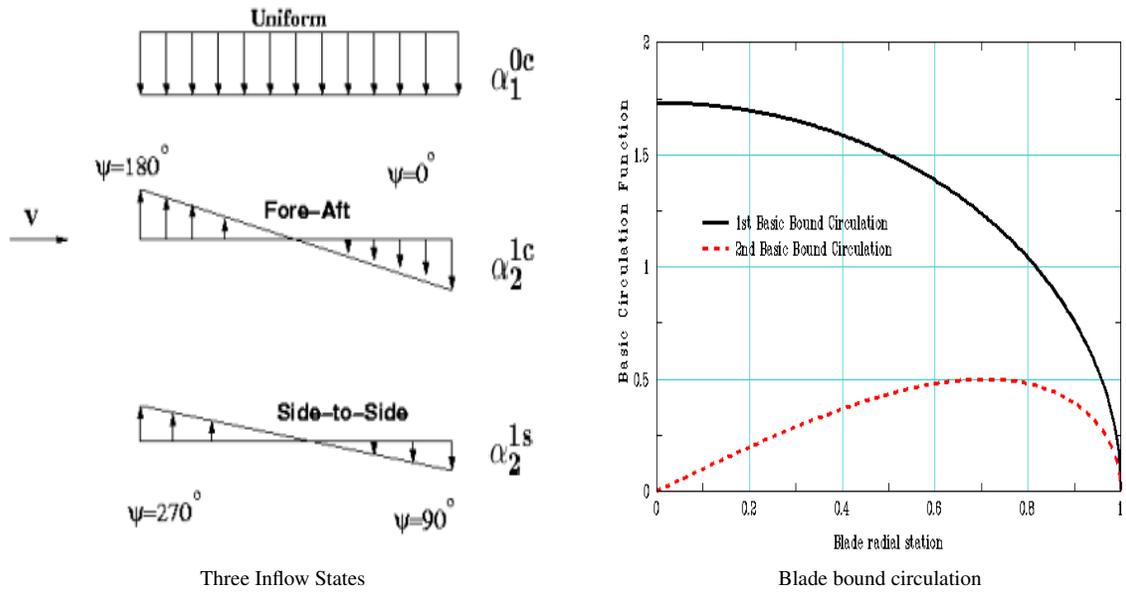
Figure 1: Illustration of 3 inflow states and basic blade bound circulation functions

Thrust Perturbation

Pitch Moment Perturbation
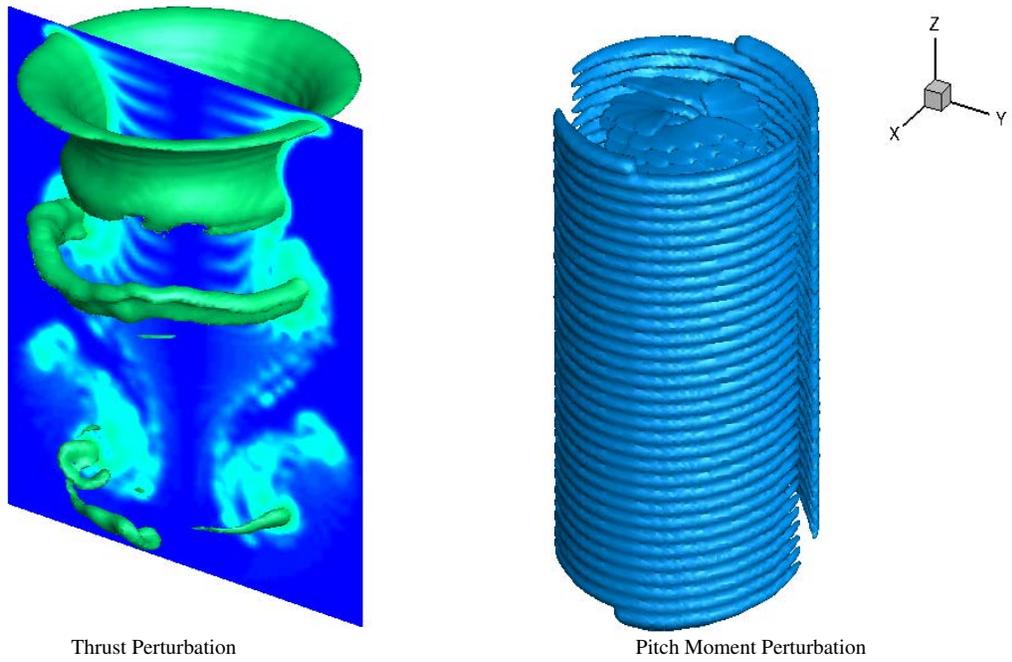
Figure 2: Rotor wake corresponding to the thrust and pitch moment perturbation in hover
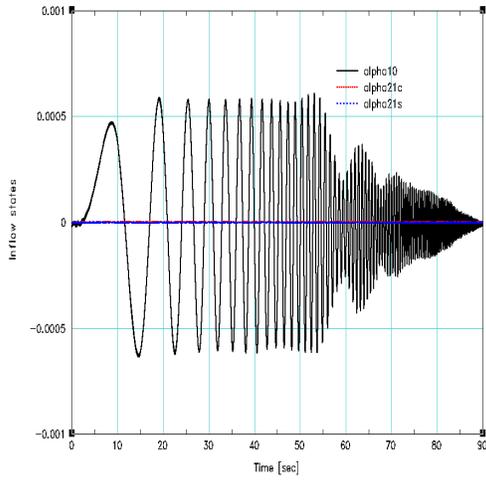
Figure 3: Inflow state response to the frequency sweep of thrust based inflow forcing function (τ_1^0) in hover
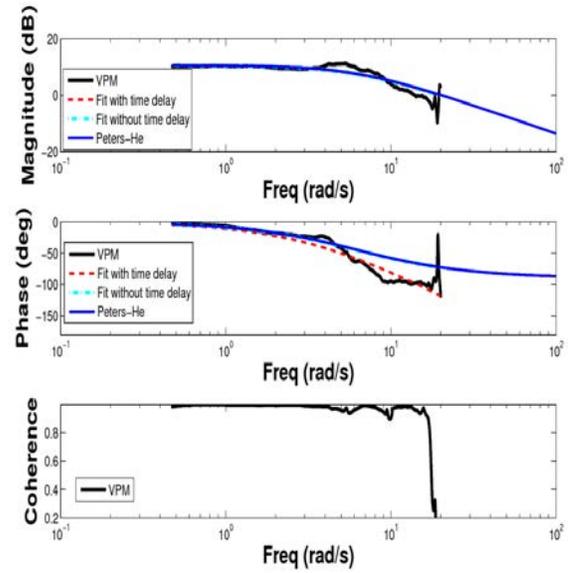
Figure 5: Frequency response of uniform inflow state to the thrust based forcing function (τ_1^0) in hover
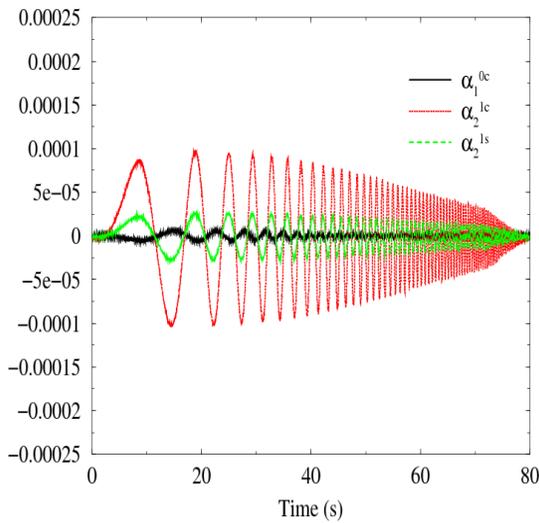
Figure 4: Inflow state response to the frequency sweep of pitch moment based inflow forcing function (τ_2^{1c}) in hover
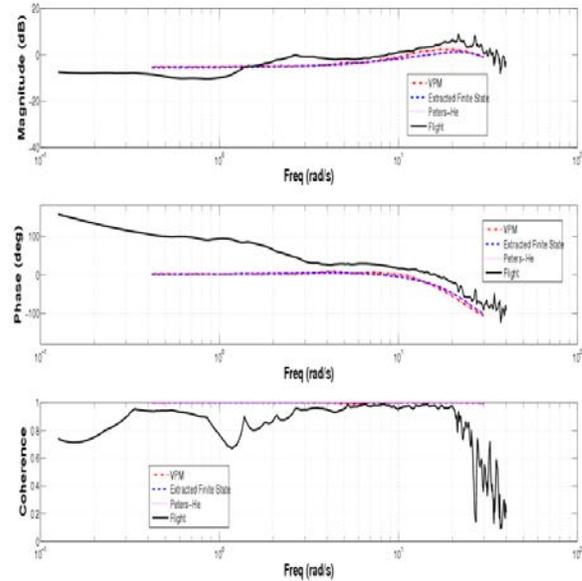
Figure 6: Frequency response of rotor coning to the frequency sweep of collective pitch in hover
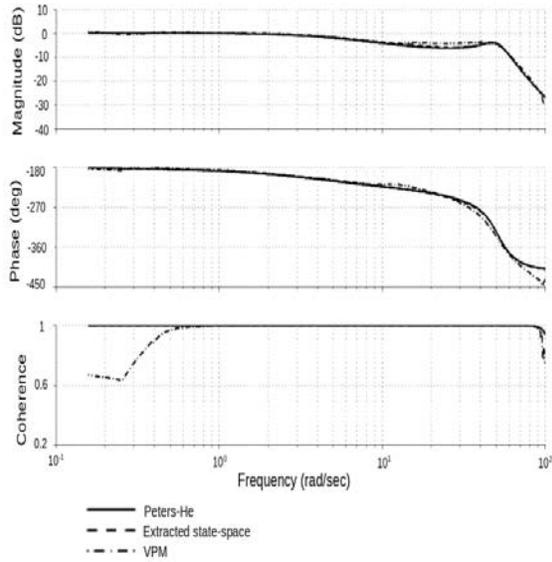
Figure 7: Frequency response of rotor longitudinal flapping to the cyclic pitch in hover
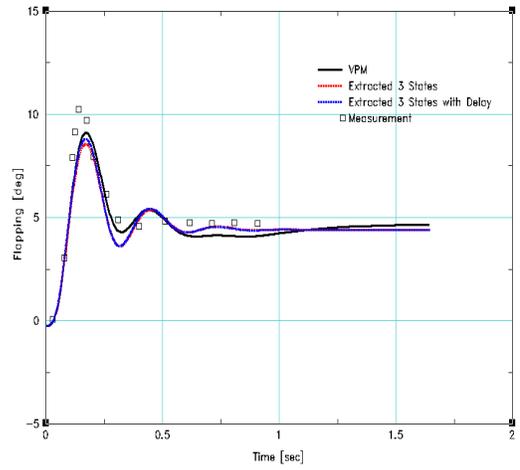
Figure 9: Rotor flapping (coning) response to the collective pull-up (200 deg/sec) in hover
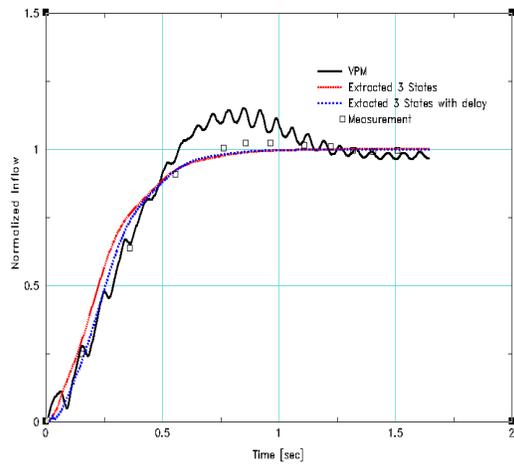
Figure 8: Rotor inflow response to the collective pull-up (200 deg/sec) in hover
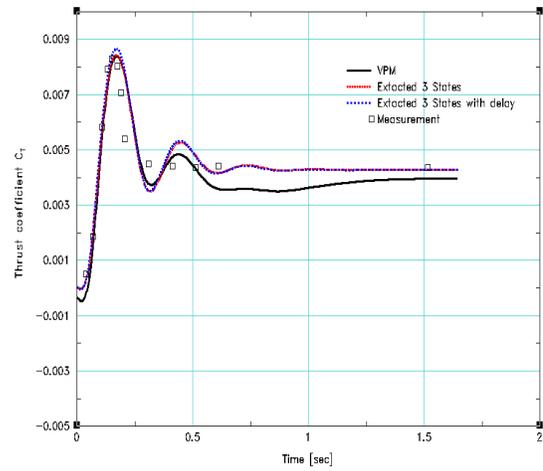
Figure 10: Rotor thrust coefficient response to the collective pull-up (200 deg/sec) in hover
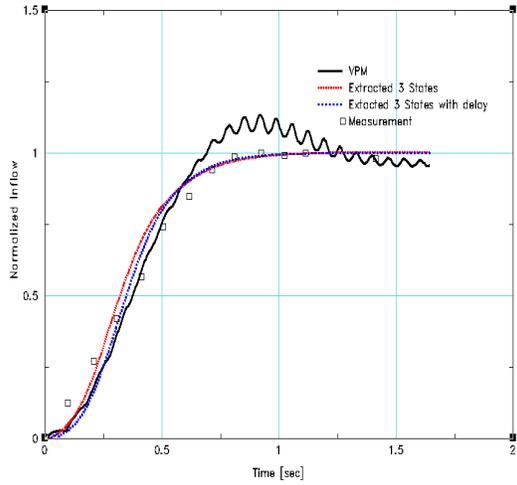
Figure 11: Rotor inflow response to the collective pull-up (48 deg/sec) in hover
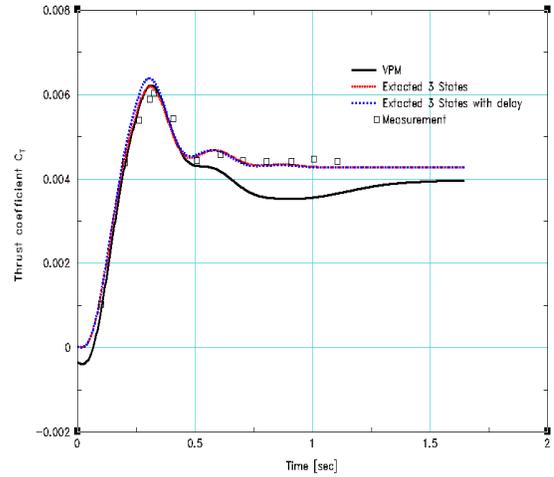
Figure 13: Rotor thrust coefficient response to the collective pull-up (48 deg/sec) in hover
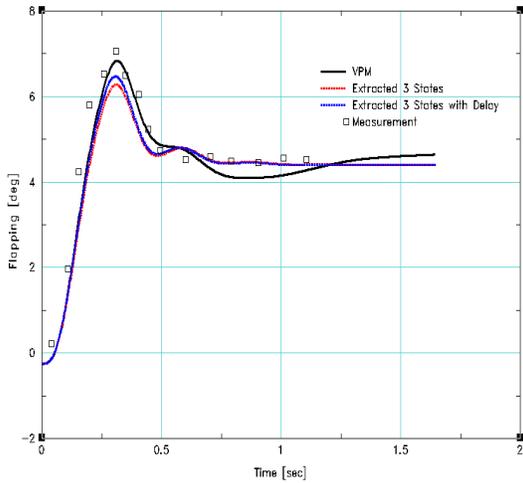
Figure 12: Rotor flapping (coning) response to the collective pull-up (48 deg/sec) in hover
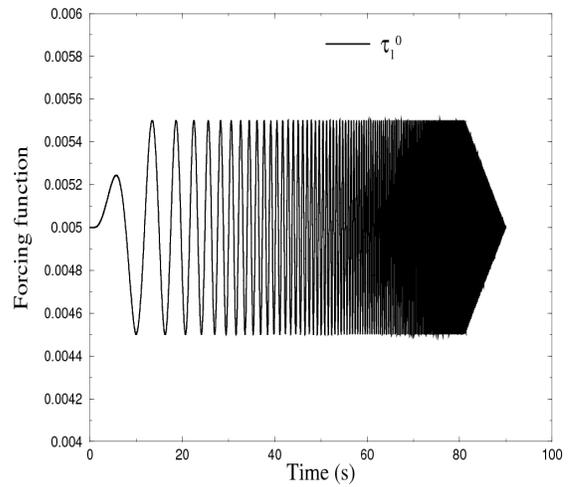
Figure 14: Sine sweep profile of rotor thrust based inflow forcing function at 80 knots

Figure 15: A Snap shoot of rotor wake vorticity iso-surface resulting from thrust based inflow forcing excitation at 80 knots
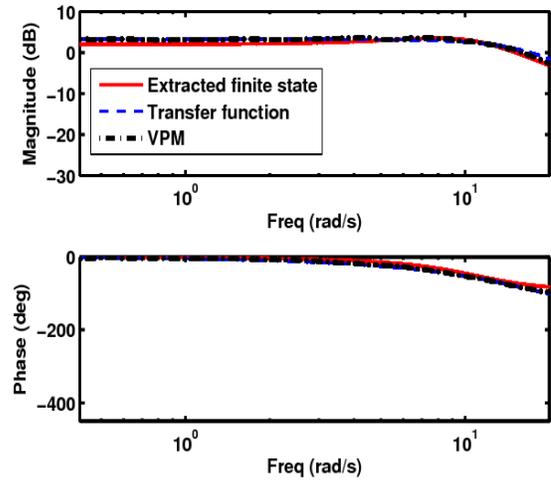
Figure 17: Comparison of frequency response of the uniform inflow state from state-space model, transfer function fit, and VPM simulation data due to thrust based excitation at 80 knots
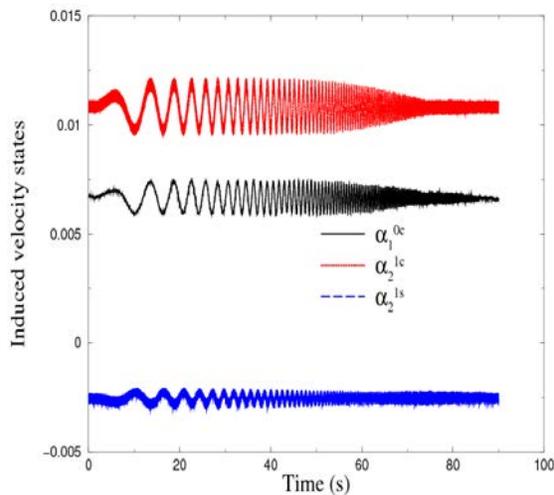
Figure 16: Rotor inflow states resulting from thrust based inflow forcing function excitation at 80 knots
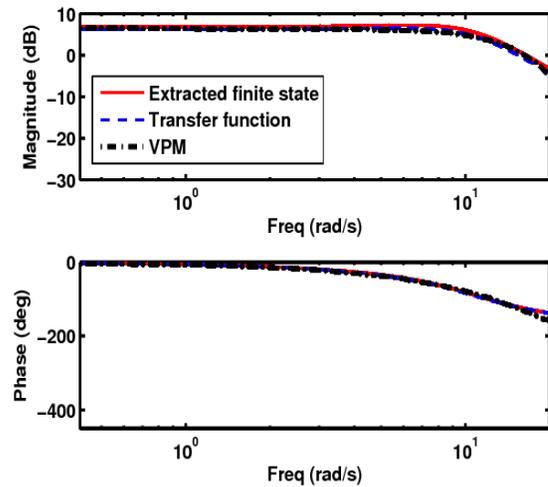
Figure 18: Comparison of frequency response of the cosine inflow state from state-space model, transfer function fit, and VPM simulation data due to thrust based excitation at 80 knots
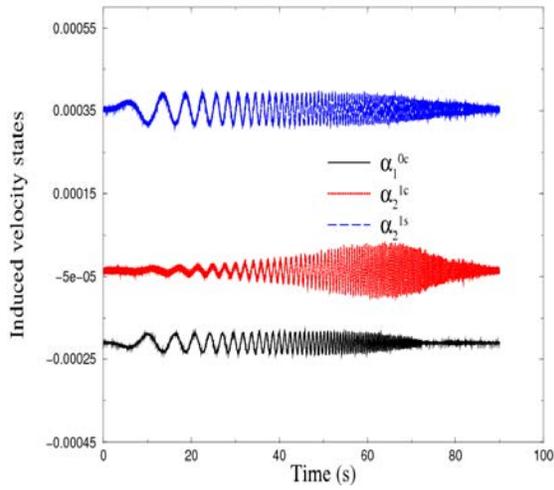
Figure 19: Rotor inflow states resulting from pitch moment based inflow forcing function (τ_2^{1c}) excitation at 80 knots
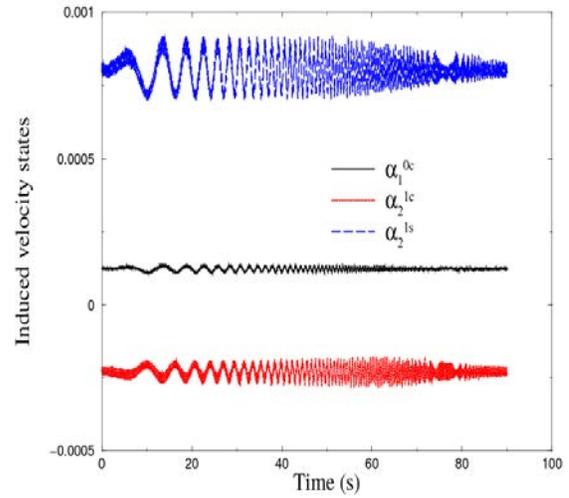
Figure 21: Rotor inflow states resulting from roll moment based inflow forcing function (τ_2^{1s}) excitation at 80 knots
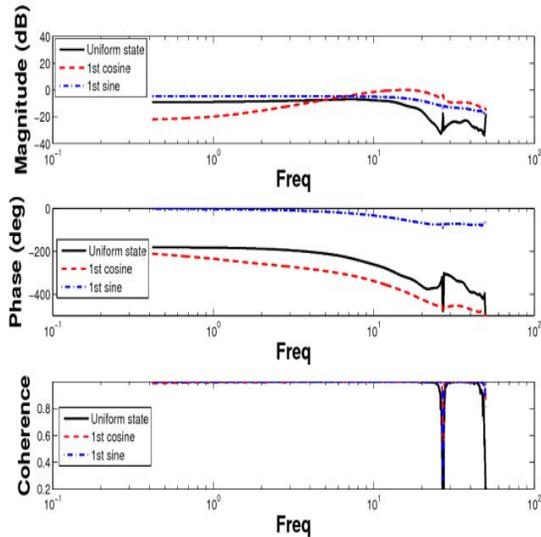
Figure 20: Frequency response of the rotor inflow states due to pitch moment based inflow forcing function (τ_2^{1c}) excitation at 80 knots
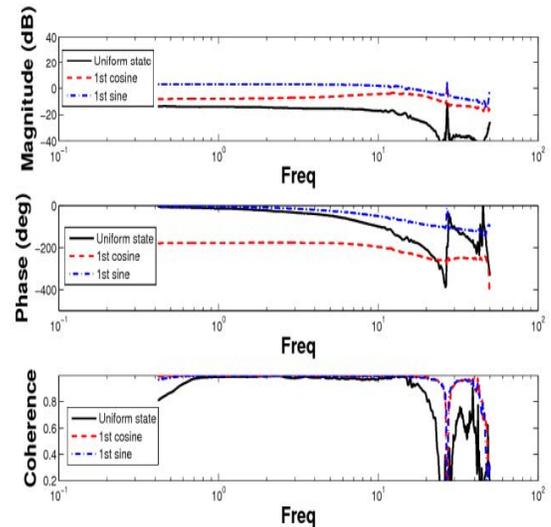
Figure 22: Frequency response of the rotor inflow states due to roll moment based inflow forcing function (τ_2^{1s}) excitation at 80 knots
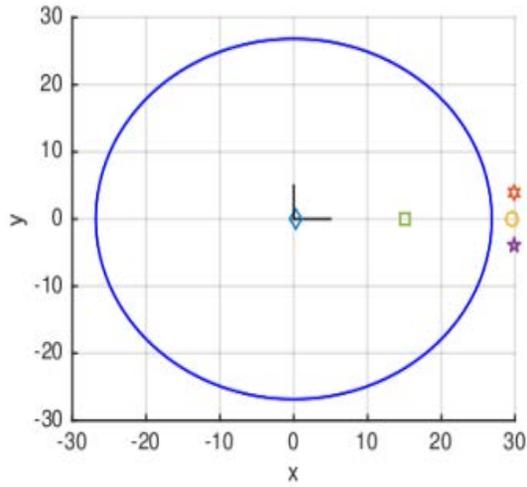
Figure 23: Illustration of flow field points selected for interference evaluation
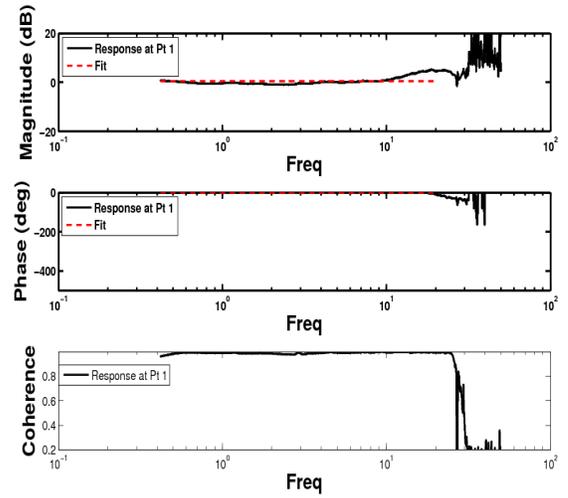
Figure 25: Frequency response of fitted rotor interference downwash at fuselage (Point 1) as compared to the VPM prediction for a sweep of thrust
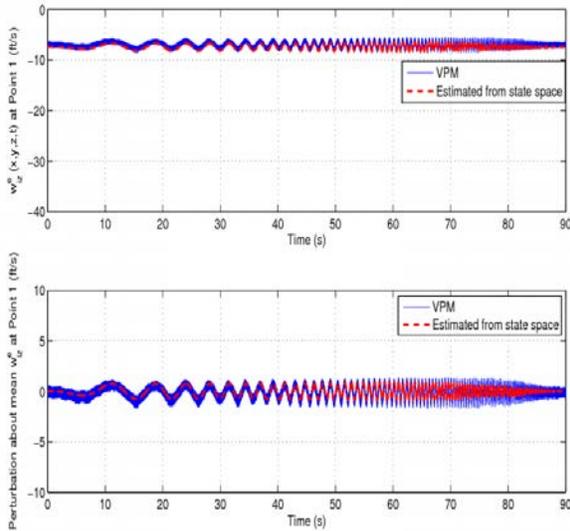
Figure 24: Time variation of fitted rotor interference downwash at fuselage (Point 1) as compared to the VPM prediction
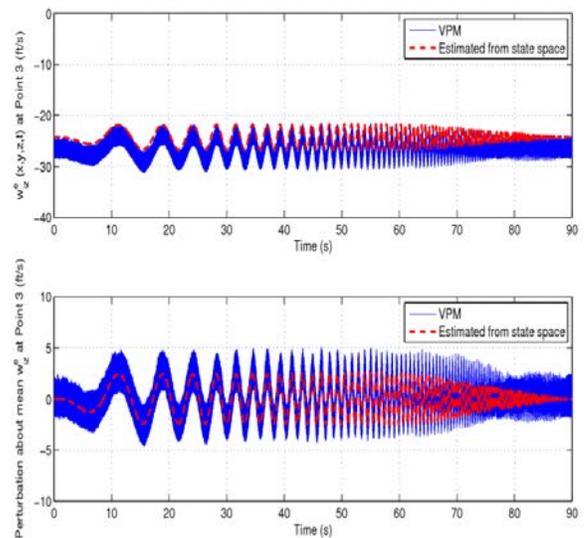
Figure 26: Time variation of fitted rotor interference downwash at vertical fin (Point 3) as compared to the VPM prediction
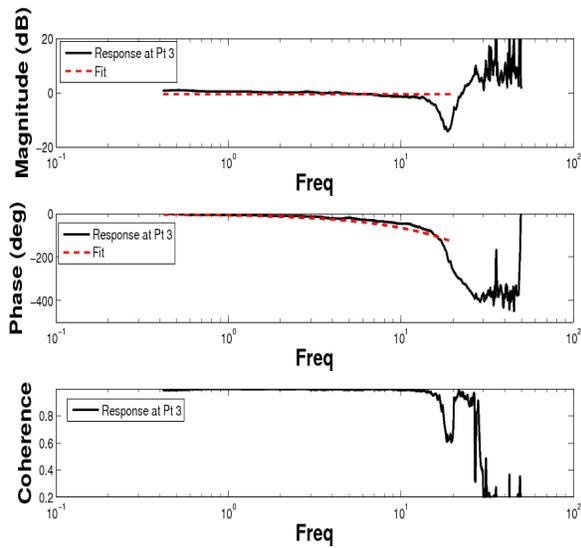
Figure 27: Frequency response of fitted rotor interference downwash at vertical fin (Point 3) as compared to the VPM prediction for a sweep of thrust
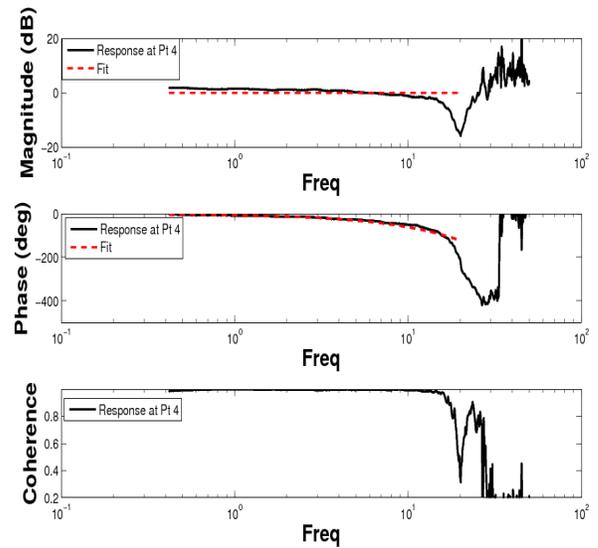
Figure 29: Frequency response of fitted rotor interference downwash at left horizontal stabilator (Point 4) as compared to the VPM prediction for a sweep of thrust
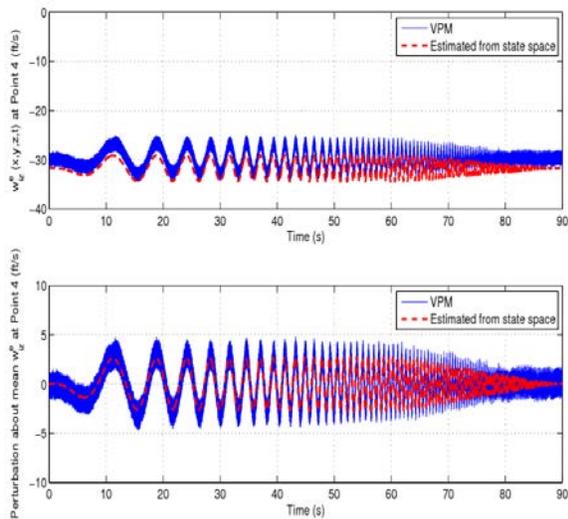
Figure 28: Time variation of fitted rotor interference downwash at left horizontal stabilator (Point 4) as compared to the VPM prediction
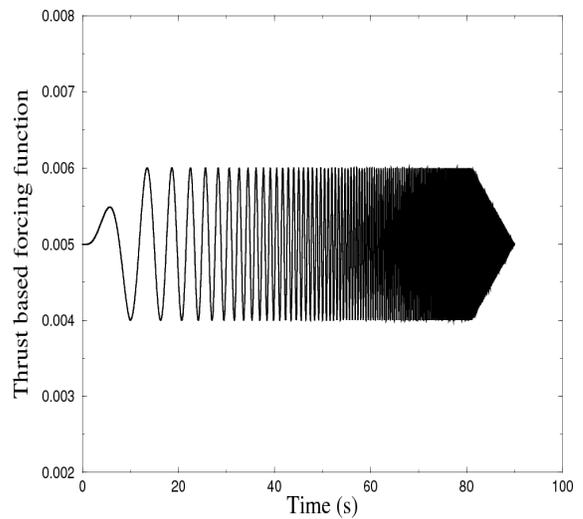
Figure 30: Time variation of the thrust based sine sweep forcing τ_1^0

x/R
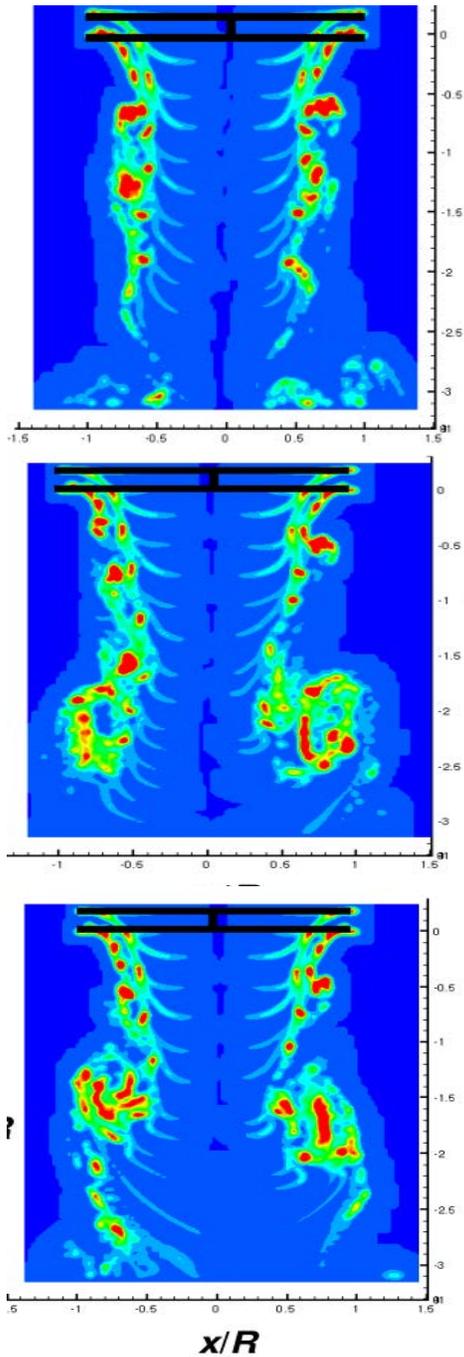
Figure 31: Comparison of the vorticity contours along the longitudinal plane passing through the rotor hub, as obtained in steady state, and at $t = 90$ s for the thrust-based sine sweep forcing applied to the upper and the lower rotors
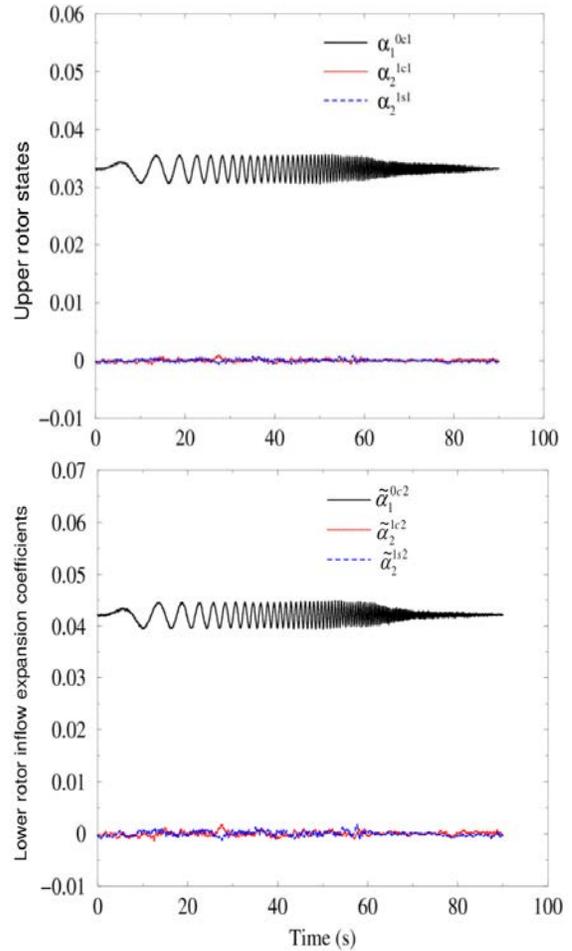
Figure 32: Upper rotor inflow states and lower rotor interference inflow expansion coefficients as obtained from the VPM simulation with the thrust sine sweep forcing τ_1^{01} applied to the upper rotor
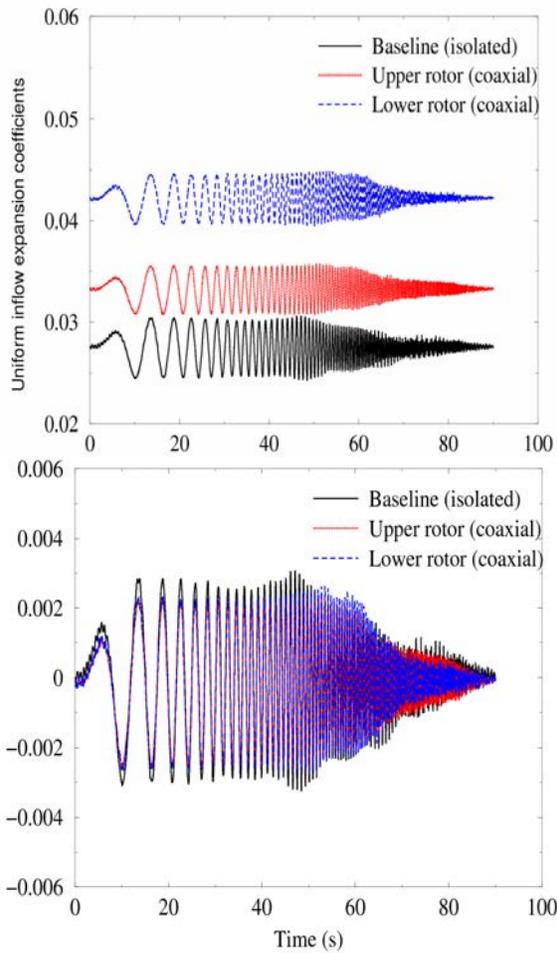
Figure 33: The time histories of the upper rotor uniform inflow state and the lower rotor uniform interference inflow expansion coefficient as obtained from the upper rotor thrust sine sweep simulation, along with the time history of the baseline rotor uniform inflow state
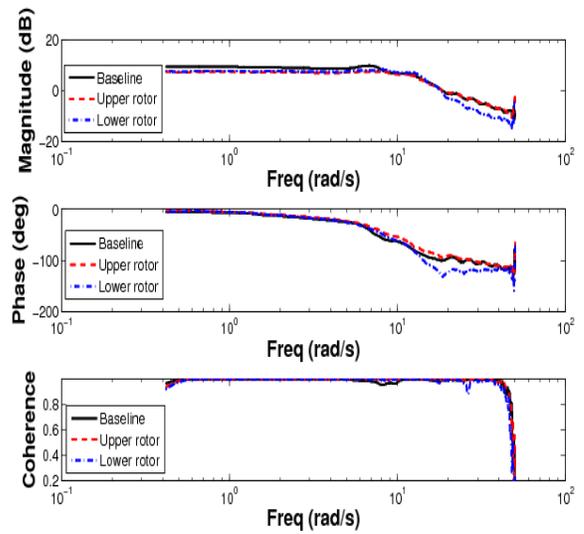
Figure 34: Frequency response of the upper rotor uniform inflow state and the lower rotor uniform interference inflow expansion coefficient as obtained from the upper rotor thrust sine sweep simulation, along with the frequency response of the baseline rotor uniform inflow state

Figure 36: Frequency responses of the upper rotor uniform inflow expansion coefficient ($\tilde{\alpha}_1^{01}$) and the lower rotor uniform inflow state (α_1^{02}) as obtained from the lower rotor thrust sine sweep simulation, along with the frequency response of baseline rotor uniform inflow state
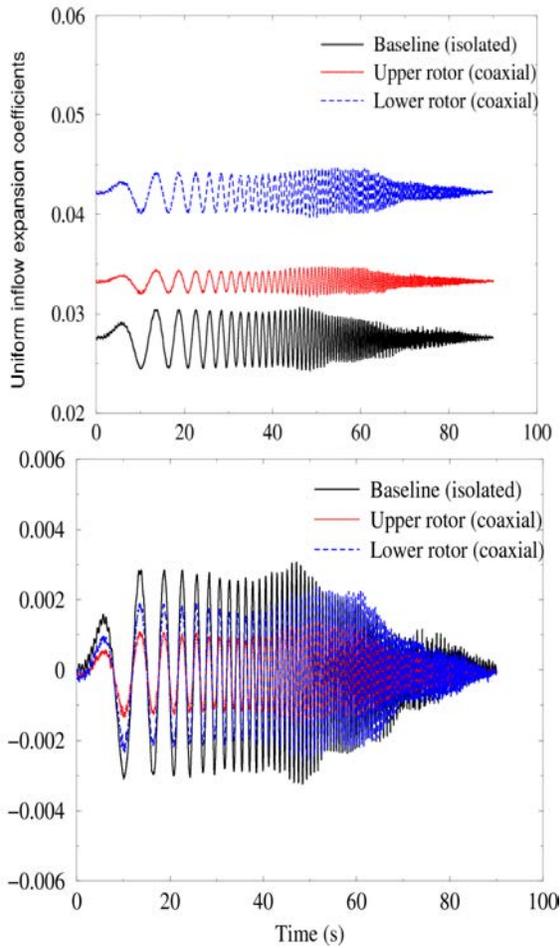
Figure 35: Time histories of the upper rotor uniform inflow expansion coefficient ($\tilde{\alpha}_1^{01}$) and lower rotor uniform inflow state (α_1^{02}) as obtained from the lower rotor thrust sine sweep simulation, along with the baseline rotor uniform inflow state variation
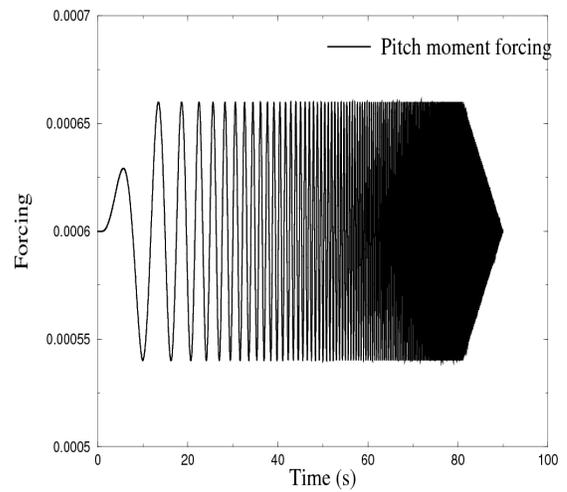
Figure 37: Time history of the pitch moment based sine sweep forcing
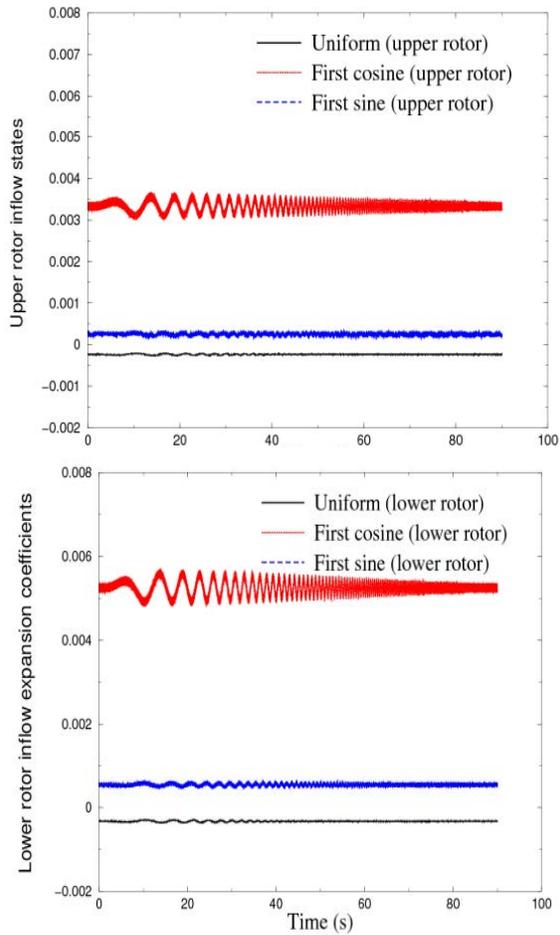
Figure 38: Upper rotor inflow states and the lower rotor interference expansion coefficients as obtained from the upper rotor pitch moment based sine sweep forcing in hover
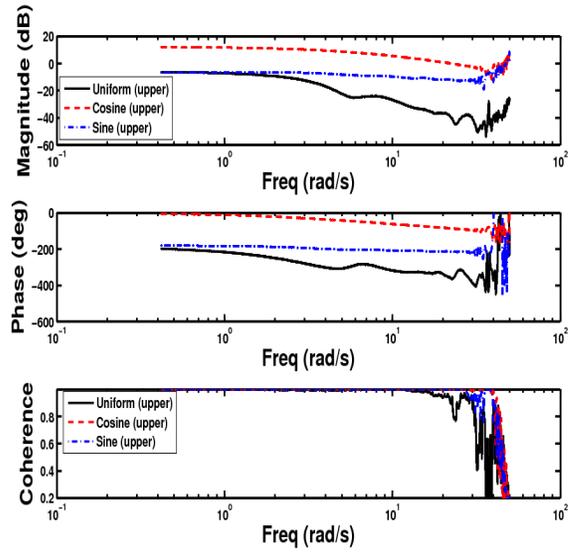
Figure 39: Frequency responses of the upper rotor inflow states as obtained from the upper rotor pitch moment sine sweep simulation (τ_2^{1c1}) in hover
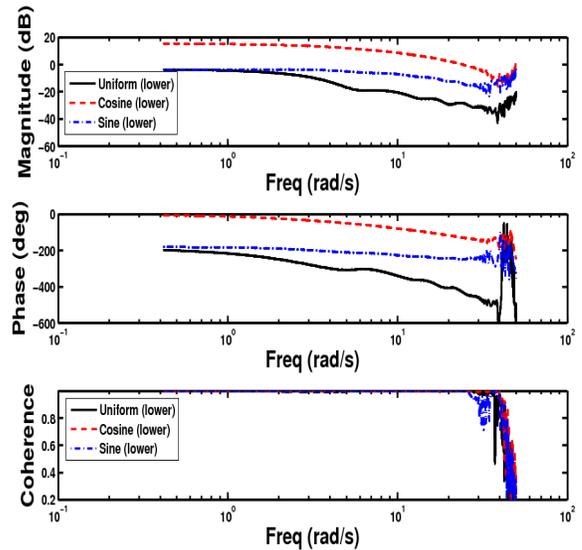
Figure 40: Frequency responses of the lower rotor inflow expansion coefficients as obtained from the upper rotor pitch moment sine sweep simulation (τ_2^{1c1}) in hover
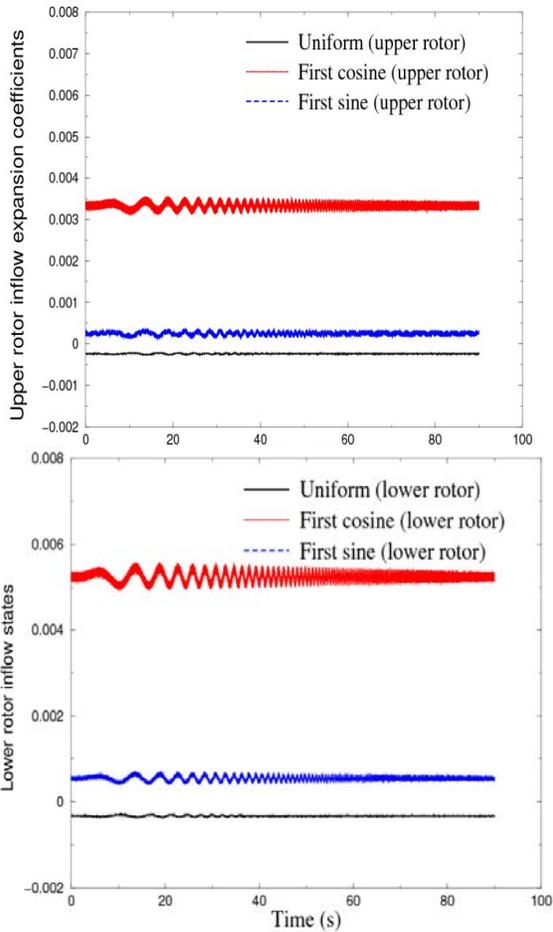
Figure 41: Upper rotor inflow expansion coefficients and the lower rotor inflow states as obtained from the lower rotor pitch moment sine sweep forcing
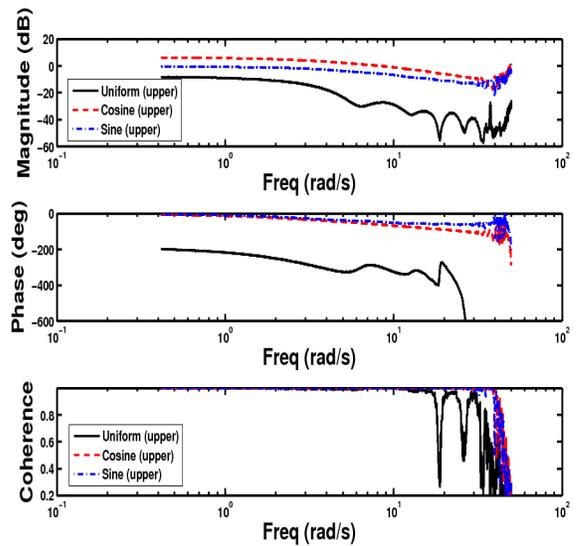
Figure 42: Frequency responses of the upper rotor inflow expansion coefficients as obtained from the lower rotor pitch moment sine sweep simulation
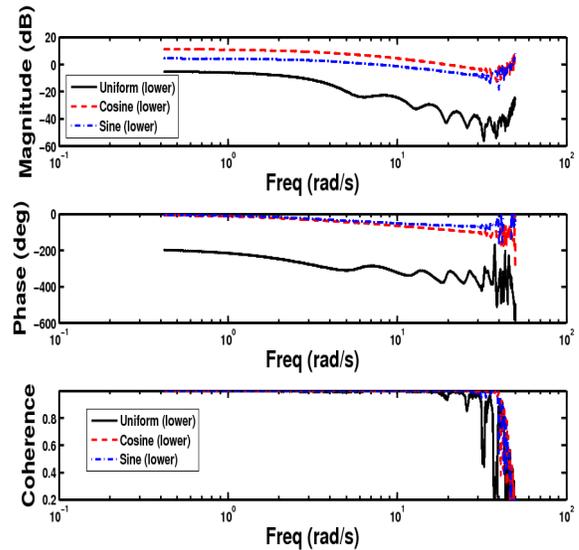
Figure 43: Frequency responses of the lower rotor inflow states as obtained from the lower rotor pitch moment sine sweep simulation
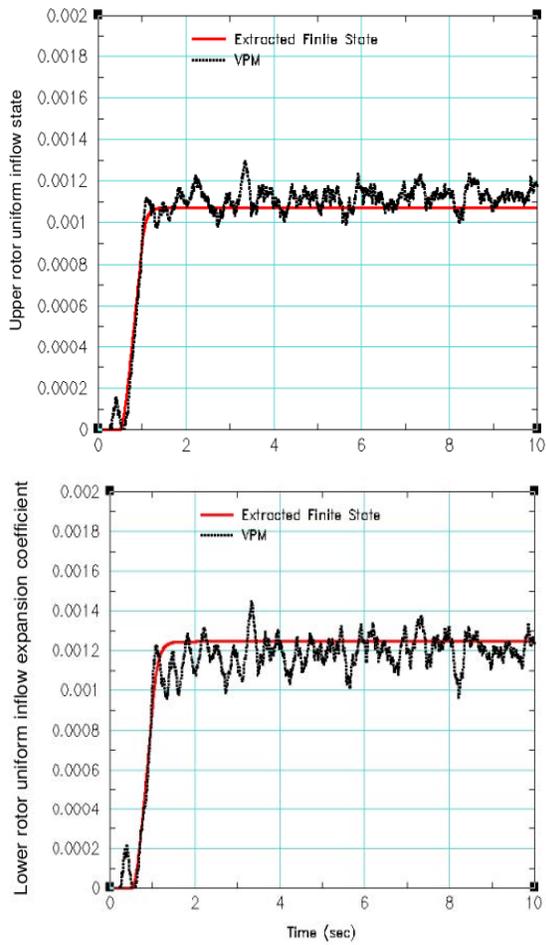
Figure 44: Upper rotor uniform inflow state and lower rotor uniform interference inflow expansion coefficients obtained as responses to a step ramp-up (0.5 sec) of thrust based inflow forcing function on the upper rotor
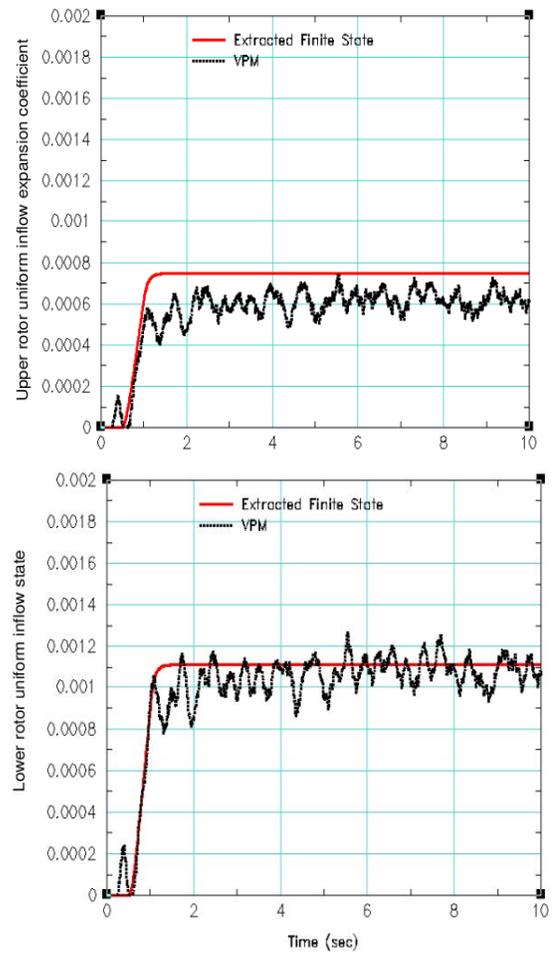
Figure 45: Upper rotor uniform inflow state and lower rotor uniform interference inflow expansion coefficient obtained as responses to a step ramp-up (0.5 sec) of thrust based inflow forcing function on the lower rotor
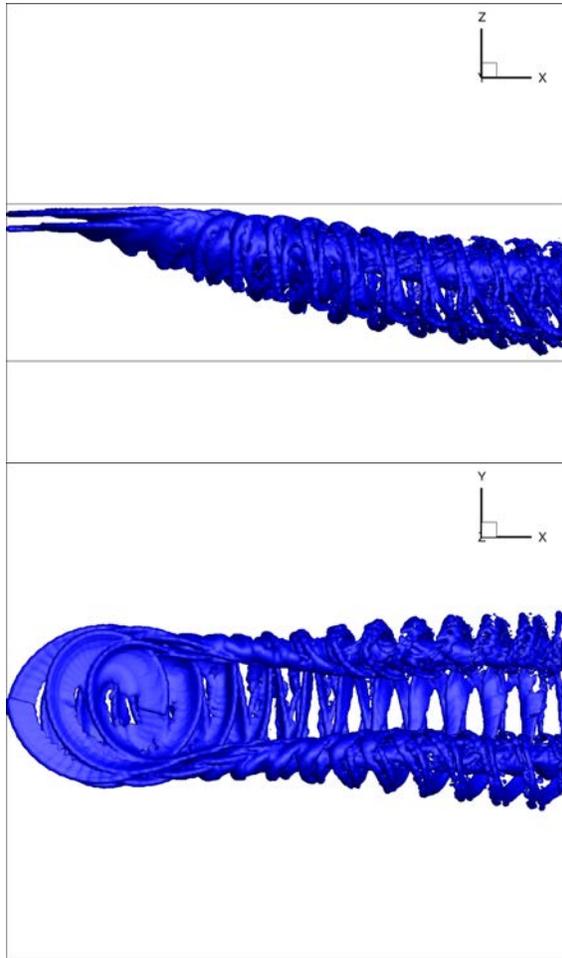
Figure 46: Side and top views of the rotor wake in steady state as obtained from a VPM simulation for a coaxial Harrington Rotor I in 40 knots forward flight
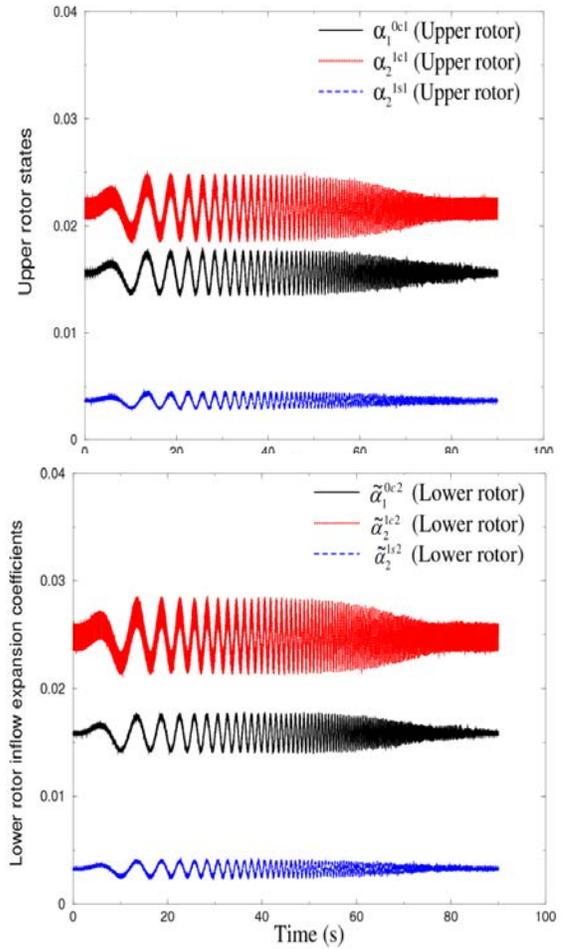
Figure 47: The upper rotor inflow states and the lower rotor interference inflow expansion coefficients as obtained from the VPM simulation with thrust sine sweep forcing applied to the upper rotor in forward flight at 40 knots
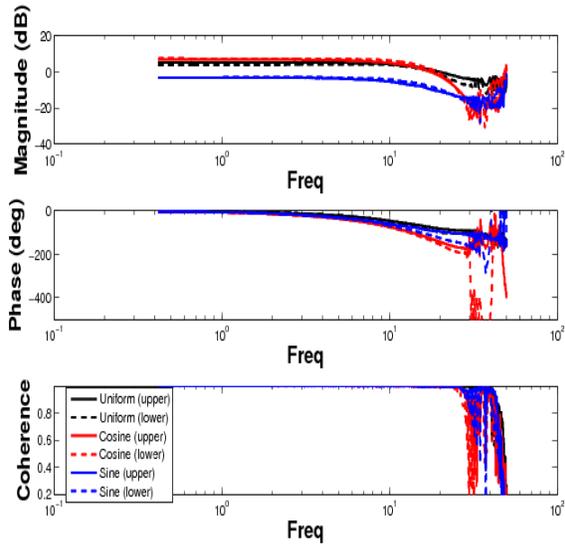
Figure 48: Frequency responses of the upper rotor states and the corresponding lower rotor inflow expansion coefficients as obtained from the upper rotor thrust sine sweep simulation in forward flight at 40 knots
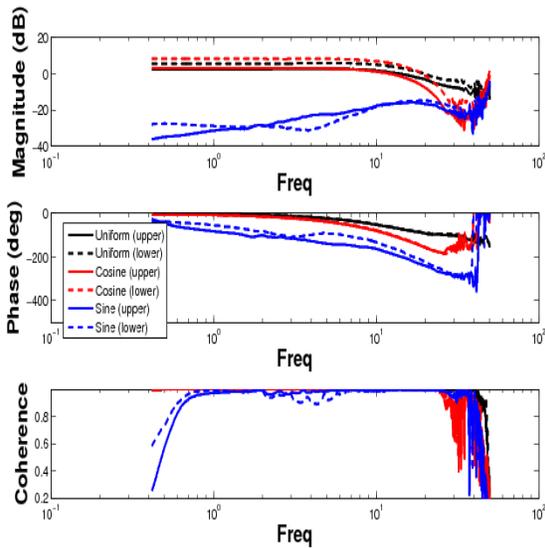
Figure 49: Frequency responses of the lower rotor inflow states and the corresponding upper rotor interference inflow expansion coefficients as obtained from the lower rotor thrust sine sweep simulation in forward flight at 40 knots